Optimal Polar Wavelet Transform for Damage Detection in Laminated Composite Circular Plates

Published Version:
Saadatmorad, M., Jafari-Talookolaei, R., Katunin, A., Fantuzzi, N., Khatir, S. (2026). Optimal Polar Wavelet Transform for Damage Detection in Laminated Composite Circular Plates. EUROPEAN JOURNAL OF MECHANICS. A, SOLIDS, 118, 1-42 [10.1016/j.euromechsol.2026.106077].

Availability:
This version is available at: https://hdl.handle.net/11585/1047131 since: 2026-02-21

Published:
DOI: http://doi.org/10.1016/j.euromechsol.2026.106077

Optimal Polar Wavelet Transform for Damage Detection in Laminated Composite Circular Plates

Morteza Saadatmorad[a], Ramazan-Ali Jafari-Talookolaei[b*], Andrzej Katunin[c], Nicholas Fantuzzi[a], Samir Khatir[d]

[a] Department of Civil, Chemical, Environmental and Materials Engineering, University of Bologna, Bologna, Italy.

[b] School of Mechanical Engineering, Babol Noshirvani University of Technology, Babol, Iran.

[c] Department of Fundamentals of Machinery Design, Faculty of Mechanical Engineering, Silesian University of Technology, Konarskiego 18A, 44-100 Gliwice, Poland.

[d] Center for Engineering Application and Technology Solutions, Ho Chi Minh City Open University, Ho Chi Minh, 700000, Vietnam

* Corresponding author: ramazanali@gmail.com, ra.jafari@nit.ac.ir

Abstract

This study introduces an optimal polar wavelet transform for damage detection in laminated composite circular plates. The core concept behind the proposed method lies in strategically selecting the most informative polar detail signals to extract damage-related information from vibration mode shapes. To guide this selection process, a minimum energy ratio (MER) index is introduced as a benchmark for identifying the most effective polar wavelet function by evaluating the energy balance between the approximation signal and the various detail signals. To generate reliable vibration data for the proposed damage detection framework, the mathematical model for the circular plate has been developed based on the first-order shear deformation theory (FSDT), neglecting damping effects to simplify the analysis. By introducing central and non-central finite elements, the solution is calculated using the finite element method (FEM), and a convergence study is conducted to verify the accuracy of the numerical model. The effects of different parameters such as location of damage, level of damage, noise, number of layers, and lay-ups on detecting the damages of laminated composite circular plates are considered numerically and experimentally. Results show that the developed optimal wavelet transform can more accurately predict the location of the damage compared to the traditional polar wavelet transform.

Keywords: Polar wavelet transform; Damage detection; Laminated composite circular plates; Experimental modal analysis.

1. Introduction

Structural health monitoring (SHM) plays a crucial role in reducing losses caused by structural damage [1–6]. SHM can be implemented at various levels. At the first level, SHM focuses on identifying the presence or absence of damage by comparing current measurements with those obtained from the healthy state of the structure. Once damage is detected, higher-level SHM

approaches can be employed to determine the location and severity of the damage [7–13].
On the other hand, laminated composite structures have many applications in various fields such as mechanical, civil, aerospace, and automotive engineering [14]. This wide application of laminated composite structures is due to their desired properties such as corrosion and fatigue resistances and high strength-to-weight ratio [15-17]. Many laminated composite structures are used in high-speed applications; as a result, they are exposed to potential damage [18-21]. Hence, applying SHM on these structures is vital [22].
Wavelet transforms are widely used for detecting damage in laminated composite structures and are effective in SHM for capturing signals and locating damage [23]. Numerous researchers have employed different versions of wavelet transforms to monitor various types of laminated composites. For example, Sohn et al. [24] used the one-dimensional continuous wavelet transform (1D-CWT) to detect delamination damage in a laminated composite plate with attached piezoelectric patches. The processed signal was Lamb waves. Grabowska et al. [25] detect damage in composite rods using the 1D-CWT. Wang et al. [26] detected delamination in cantilever beams. Deflection of the beam was obtained using a high-precision laser sensor as the input signal of the 1D-CWT. The Gabor wavelet was selected as the analyzing wavelet. The approach effectively detected and located delamination within the beam structures. Yang et al. [27] combined the 1D-CWT and Fourier transform for detecting cracks in laminated composite beams. The signal analyzed in this study was in vibration mode shapes. Their results showed that the proposed approach effectively detected damage in noisy conditions, without knowing prior knowledge about material properties and damage location.
These investigations utilized the one-dimensional continuous wavelet transform (1D-CWT). While, another method, the one-dimensional discrete wavelet transform (1D-DWT), offers the advantage of decomposing the signal into detail and approximation sub-signals, allowing for the detection of structural damage in the detail signal. Note that the 1D-CWT is not a decomposition-based wavelet transform and for detecting damage, the higher scales of 1D-CWT are redundant. Sung et al. [28] identified internal damage in composite plates subjected to low-speed impacts using 1D-DWT.
Another most commonly used version of wavelet transform for structural damage detection is two-dimensional discrete wavelet transform (2D-DWT). Katunin et al. [29] introduced a new damage detection algorithm using 2D-DWT to detect damage in a geometrically non-linear composite blade. This algorithm outperformed other wavelet transforms, even under noisy conditions. Katunin and Przystałka [30] developed a sensitive method for detecting damage in composite plates using the fractional discrete wavelet transform (FDWT). Various optimization algorithms were employed to determine the optimal FDWT parameters. Their results showed that the optimized FDWT presented

high-accuracy damage detection in composite structures. Knitter-Piątkowska et al. [31] employed 1D-DWT and 2D-DWT to detect cracks in composite plates, which were subjected to static and dynamic loading to generate signals for wavelet transform analysis. Finally, the two-dimensional continuous wavelet transform (2D-CWT) is another type most commonly used for detecting damage in laminated composite structures. For example, Fan et al. [32] applied the 2D-CWT to detect damage in plate structures. The wavelet Dergauss2d analyzed the original signal to obtain wavelet coefficients. The concept of Isosurfaces of the 2D-CWT coefficients was suggested as a damage detection index. Results showed that the proposed algorithm can effectively detect damage in plate-like structures.

Most of the structures studied in previous research on the application of wavelet transforms in structural damage detection had a rectangular-wise geometry. Therefore, the data acquisition for processing had a linear arrangement. However, sometimes, the structure under analysis is circular; thus, the signal acquisition is performed based on the circular arrangement of the sensors. In such cases, the polar wavelet transform can be used to detect damage in circular structures. Trendafoilova et al. [33] noted that frequency-based methods have limitations in detecting damage, making time-frequency methods essential for identifying structural issues. They used large amplitude vibrations and nonlinear time series analysis to detect damage in circular plates at low levels and noisy conditions. Tufoi et al. [34] explored damage detection in circular plates through vibration analysis by assessing mode shape characteristics. Pai et al. [35] utilized scanning laser vibrometer data to identify defects, finding that high-frequency operational deflection shapes are crucial for locating small defects in circular plates. Rathod et al. [36] introduced a method for quickly localizing corrosion damage using a circular array of piezoelectric wafer active sensors to generate and receive ultrasonic Lamb waves, effectively identifying corrosion pit locations relative to nearby sensors. Wang et al. [37] developed a technique for rapid crack quantification with a circular sensor array for Lamb wave transmission and reception, demonstrating the potential for significantly enhancing crack assessment accuracy in plate-like structures. Giridhara et al. [38] presented a new damage detection method for structures via a circular array of piezoelectric wafer active sensors. Results showed that the proposed method was a robust and efficient approach for damage assessment in plate structures by effectively analyzing Lamb wave propagation patterns within a circular sensor array.

As the only and closest study to this work, Katunin [39] studied damage detection in circular glass-epoxy laminate composites using the polar discrete wavelet transform (PDWT). The research modeled four types of damage: radial cracks, circumferential cracks, voids, and delamination within a finite element framework to evaluate detection accuracy. The algorithm focused on identifying singularities in the axial displacements of the structure's natural vibration modes. The results confirmed PDWT's effectiveness in precise identification damage in circular composite structures, positioning it as a valuable tool for structural diagnostics.

This paper proposes an index for selecting optimal polar wavelet functions to enhance damage detection in laminated composite discs. The criterion focuses on minimizing the ratio of approximation coefficient energy to the total energy of radial, angular, and coupled details. In this way, the ratio of the energy of the approximation signal to the radial details, the ratio of the energy of the approximation signal to the angular details, and the ratio of the energy of the approximation signal to the coupled details, known as the MER index, are compared with each other for different wavelet functions and three different types of detail signals to obtain the optimal details and wavelet function for the polar wavelet transform. Then, using them, damage scenarios are investigated to compare the performance of the proposed methodology with the conventional polar wavelet transform method. Therefore, this paper presents a new method for selecting the optimal detail signal and the optimal wavelet function to increase the accuracy of damage detection and reduce the dependence of the conventional polar wavelet transform on the selection of the wavelet function based on trial-and-error simulations.

2. Mathematical Model

Consider a laminated composite circular plate, as shown in Fig. 1. As depicted, the plate has the radius R and the thickness h. The coordinate system (r, θ, z) is assumed to be centered at the center of the plate, and as shown in Fig. 1, the deformation of the points on the plate is represented by the variables (u, v, w), respectively. The plate consists of N layers, where the position of the top and bottom of the k^{th} layer relative to the middle plane is specified by z_{k+1} and z_k.

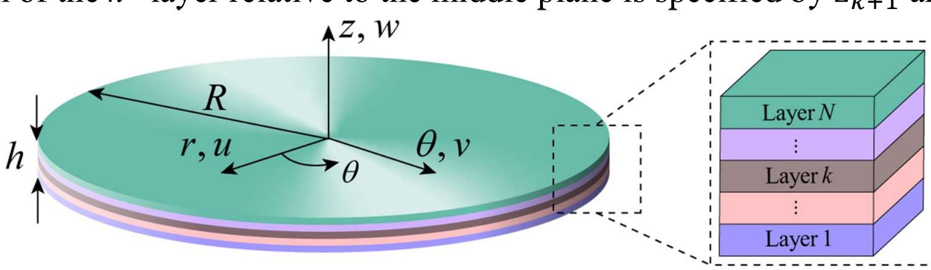

Fig. 1: Schematic view of a laminated composite circular plate

Based on the FSDT, the displacement field in the plate is written as follows:

$$
\begin{aligned}
u(r,\theta,z,t) &= u_0(r,\theta,t) + z\,\psi_r(r,\theta,t) \\
v(r,\theta,z,t) &= v_0(r,\theta,t) + z\,\psi_\theta(r,\theta,t) \\
w(r,\theta,z,t) &= w_0(r,\theta,t)
\end{aligned}
\tag{1}
$$

where t represents time. Using the strain-displacement relations, the non-zero strains can be calculated as follows:

$$
\varepsilon_r = \varepsilon_r^0 + z\,\kappa_r \tag{2}
$$

$$\varepsilon_\theta = \varepsilon_\theta^0 + z\,\kappa_\theta$$
$$\gamma_{r\theta} = \gamma_{r\theta}^0 + z\,\kappa_{r\theta}$$
$$\gamma_{rz} = w_{0,r} + \psi_r$$
$$\gamma_{\theta z} = \frac{w_{0,\theta}}{r} + \psi_\theta$$

in which:

$$\varepsilon_r^0 = u_{0,r}, \qquad \kappa_r = \psi_{r,r}$$
$$\varepsilon_\theta^0 = \frac{u_0 + v_{0,\theta}}{r}, \qquad \kappa_\theta = \frac{\psi_r + \psi_{\theta,\theta}}{r} \tag{3}$$
$$\gamma_{r\theta}^0 = \frac{u_{0,\theta} - v_0}{r} + v_{0,r}, \qquad \kappa_{r\theta} = \frac{\psi_{r,\theta} - \psi_\theta}{r} + \psi_{\theta,r}$$

It is worth noting that in the above relations and the following relations, comma denotes the derivative with respect to the parameter that appears after it. The kinetic energy in the plate is written as follows:

$$T = \frac{1}{2}\int_V \rho\left(u_{,t}{}^2 + v_{,t}{}^2 + w_{,t}{}^2\right)dV$$
$$= \frac{1}{2}\int_0^R \left(\int_0^{2\pi}\left(\int_{-\frac{h}{2}}^{\frac{h}{2}} \rho\left(u_{,t}{}^2 + v_{,t}{}^2 + w_{,t}{}^2\right)dz\right)d\theta\right) r dr \tag{4}$$

where ρ is the density of the layers of the plate. By substituting the displacement field (1) into Eq. (4), we will have:

$$T = \frac{1}{2}\int_0^R \int_0^{2\pi} \left[I_1\left(u_{0,t}{}^2 + v_{0,t}{}^2 + w_{0,t}{}^2\right) + 2I_2\left(u_{0,t}\,\psi_{r,t} + v_{0,t}\,\psi_{\theta,t}\right) + I_3\left(\psi_{r,t}{}^2 + \psi_{\theta,t}{}^2\right)\right] d\theta\ r dr \tag{5}$$

where:

$$(I_1, I_2, I_3) = \sum_{k=1}^{N} \int_{z_k}^{z_{k+1}} \rho^k (1, z, z^2)\, dz \tag{6}$$

in which ρ^k is the density of the k^{th} layer. The stress-strain relation in the k^{th} layer is written as follows:

$$\begin{Bmatrix} \sigma_r \\ \sigma_\theta \\ \tau_{r\theta} \end{Bmatrix}^{(k)} = \begin{bmatrix} \bar{Q}_{11} & \bar{Q}_{12} & \bar{Q}_{16} \\ \bar{Q}_{12} & \bar{Q}_{22} & \bar{Q}_{26} \\ \bar{Q}_{16} & \bar{Q}_{26} & \bar{Q}_{66} \end{bmatrix}^{(k)} \begin{Bmatrix} \varepsilon_r \\ \varepsilon_\theta \\ \gamma_{r\theta} \end{Bmatrix}^{(k)} \tag{7-a}$$

$$\begin{Bmatrix} \tau_{\theta z} \\ \tau_{rz} \end{Bmatrix}^{(k)} = \begin{bmatrix} \bar{Q}_{44} & \bar{Q}_{45} \\ \bar{Q}_{45} & \bar{Q}_{55} \end{bmatrix}^{(k)} \begin{Bmatrix} \gamma_{\theta z} \\ \gamma_{rz} \end{Bmatrix}^{(k)} \tag{7-b}$$

where $\bar{Q}_{ij}$ $(i, j = 1,2,6\ and\ 4,5)$ are the reduced stiffness coefficients. The strain potential energy of the plate is also as follows:

$$U = \frac{1}{2}\int_V \left(\sigma_r\varepsilon_r + \sigma_\theta\varepsilon_\theta + \tau_{r\theta}\gamma_{r\theta} + \tau_{\theta z}\gamma_{\theta z} + \tau_{rz}\gamma_{rz}\right)dV \tag{8}$$

By substituting the strains from Eq. (2), the resultant forces and moments can be defined as follows:

$$(N_r, N_\theta, N_{r\theta}, Q_{\theta z}, Q_{rz}) = \int_{-\frac{h}{2}}^{\frac{h}{2}} (\sigma_r, \sigma_\theta, \tau_{r\theta}, \tau_{\theta z}, \tau_{rz})\, dz \tag{9-a}$$

$$(M_r, M_\theta, M_{r\theta}) = \int_{-\frac{h}{2}}^{\frac{h}{2}} (\sigma_r, \sigma_\theta, \tau_{r\theta})\, z\, dz \tag{9-b}$$

which are related to the strains as follows:

$$\begin{Bmatrix} N_r \\ N_\theta \\ N_{r\theta} \\ M_r \\ M_\theta \\ M_{r\theta} \end{Bmatrix} = \begin{bmatrix} A_{11} & A_{12} & A_{16} & B_{11} & B_{12} & B_{16} \\ A_{12} & A_{22} & A_{26} & B_{12} & B_{22} & B_{26} \\ A_{16} & A_{26} & A_{66} & B_{16} & B_{26} & B_{66} \\ B_{11} & B_{12} & B_{16} & D_{11} & D_{12} & D_{16} \\ B_{12} & B_{22} & B_{26} & D_{12} & D_{22} & D_{26} \\ B_{16} & B_{26} & B_{66} & D_{16} & D_{26} & D_{66} \end{bmatrix} \begin{Bmatrix} \varepsilon_r^0 \\ \varepsilon_\theta^0 \\ \gamma_{r\theta}^0 \\ \kappa_r \\ \kappa_\theta \\ \kappa_{r\theta} \end{Bmatrix} \tag{10-a}$$

$$\begin{Bmatrix} Q_{\theta z} \\ Q_{rz} \end{Bmatrix} = \begin{bmatrix} A_{44} & A_{45} \\ A_{45} & A_{55} \end{bmatrix} \begin{Bmatrix} \gamma_{\theta z} \\ \gamma_{rz} \end{Bmatrix} \tag{10-b}$$

in which:

$$\left(A_{ij}, B_{ij}, D_{ij}\right) = \sum_{k=1}^{N} \int_{z_k}^{z_{k+1}} \bar{Q}_{ij}^{\ k} (1, z, z^2)\, dz \qquad (i, j = 1,2,6 \ and \ 4,5) \tag{11}$$

By substituting Eq. (9) into Eq. (8), the strain potential energy of the plate can be written as follows:

$$\begin{aligned} U = \frac{1}{2} \int_0^R \int_0^{2\pi} \big(& N_r\, \varepsilon_r^0 + N_\theta\, \varepsilon_\theta^0 + N_{r\theta}\, \gamma_{r\theta}^0 + M_r\, \kappa_r + M_\theta\, \kappa_\theta + M_{r\theta}\, \kappa_{r\theta} \\ & + Q_{\theta z} \gamma_{\theta z} + Q_{rz} \gamma_{rz} \big)\, d\theta\ r\, dr \end{aligned} \tag{12}$$

By substituting Eqs. (3) and (10) into Eq. (12), the strain potential energy of the circular plate can be obtained in terms of the displacement field variables as follows:

$$
\begin{aligned}
U = \frac{1}{2}\int_0^R \int_0^{2\pi} \Bigg[& A_{11} {u_{0,r}}^2 + A_{22}\left(\frac{u_0 + v_{0,\theta}}{r}\right)^2 + A_{66}\left(\frac{u_{0,\theta} - v_0}{r} + v_{0,r}\right)^2 + D_{11}{\psi_{r,r}}^2 \\
& + D_{22}\left(\frac{\psi_r + \psi_{\theta,\theta}}{r}\right)^2 + D_{66}\left(\frac{\psi_{r,\theta} - \psi_\theta}{r} + \psi_{\theta,r}\right)^2 \\
& + 2A_{12}\, u_{0,r}\left(\frac{u_0 + v_{0,\theta}}{r}\right) + 2A_{16} u_{0,r}\left(\frac{u_{0,\theta} - v_0}{r} + v_{0,r}\right) \\
& + 2B_{11}\, u_{0,r}\, \psi_{r,r} + 2B_{12} u_{0,r}\left(\frac{\psi_r + \psi_{\theta,\theta}}{r}\right) \\
& + 2B_{16} u_{0,r}\left(\frac{\psi_{r,\theta} - \psi_\theta}{r} + \psi_{\theta,r}\right) \\
& + 2A_{26}\left(\frac{u_0 + v_{0,\theta}}{r}\right)\left(\frac{u_{0,\theta} - v_0}{r} + v_{0,r}\right) + 2B_{12}\left(\frac{u_0 + v_{0,\theta}}{r}\right)\psi_{r,r} \\
& + 2B_{22}\left(\frac{u_0 + v_{0,\theta}}{r}\right)\left(\frac{\psi_r + \psi_{\theta,\theta}}{r}\right) \\
& + 2B_{26}\left(\frac{u_0 + v_{0,\theta}}{r}\right)\left(\frac{\psi_{r,\theta} - \psi_\theta}{r} + \psi_{\theta,r}\right) \\
& + 2B_{16}\psi_{r,r}\left(\frac{u_{0,\theta} - v_0}{r} + v_{0,r}\right) \\
& + 2B_{26}\left(\frac{u_{0,\theta} - v_0}{r} + v_{0,r}\right)\left(\frac{\psi_r + \psi_{\theta,\theta}}{r}\right) \\
& + 2B_{66}\left(\frac{u_{0,\theta} - v_0}{r} + v_{0,r}\right)\left(\frac{\psi_{r,\theta} - \psi_\theta}{r} + \psi_{\theta,r}\right) \\
& + 2D_{12}\psi_{r,r}\left(\frac{\psi_r + \psi_{\theta,\theta}}{r}\right) + 2D_{16}\psi_{r,r}\left(\frac{\psi_{r,\theta} - \psi_\theta}{r} + \psi_{\theta,r}\right) \\
& + 2D_{26}\left(\frac{\psi_r + \psi_{\theta,\theta}}{r}\right)\left(\frac{\psi_{r,\theta} - \psi_\theta}{r} + \psi_{\theta,r}\right) + A_{44}\left(\frac{w_{0,\theta}}{r} + \psi_\theta\right)^2 \\
& + A_{55}\left(w_{0,r} + \psi_r\right)^2 + 2A_{45}\left(\frac{w_{0,\theta}}{r} + \psi_\theta\right)\left(w_{0,r} + \psi_r\right)\Bigg] d\theta\ r dr
\end{aligned} \tag{13}
$$

3. Solution Method

In the present work, the finite element method is used to calculate the response of the system. Two types of elements are considered in this paper, as shown in Fig. 2, one of which is central and the other is non-central. The central element has 7 nodes, and the non-central element has 9 nodes (Fig. 2). Each node in both elements has 5 degrees of freedom, including $(u_0, v_0, w_0, \psi_r, \psi_\theta)$. The vector of degrees of freedom for the elements is written as follows:

Central element:

$$\{\Delta_e\} = \{[\delta_1], [\delta_2], [\delta_3], [\delta_4], [\delta_5], [\delta_6], [\delta_7]\}^T \tag{14}$$

Non-central element:

$$\{\Delta_e\} = \{[\delta_1], [\delta_2], [\delta_3], [\delta_4], [\delta_5], [\delta_6], [\delta_7], [\delta_8], [\delta_9]\}^T \tag{15}$$

where $[\delta_i]$ (i=1-9) represents the degrees of freedom of each node:

$$[\delta_i] = [u_{0i}, v_{0i}, w_{0i}, \psi_{ri}, \psi_{\theta i}] \qquad (i = 1 - 9) \tag{16}$$

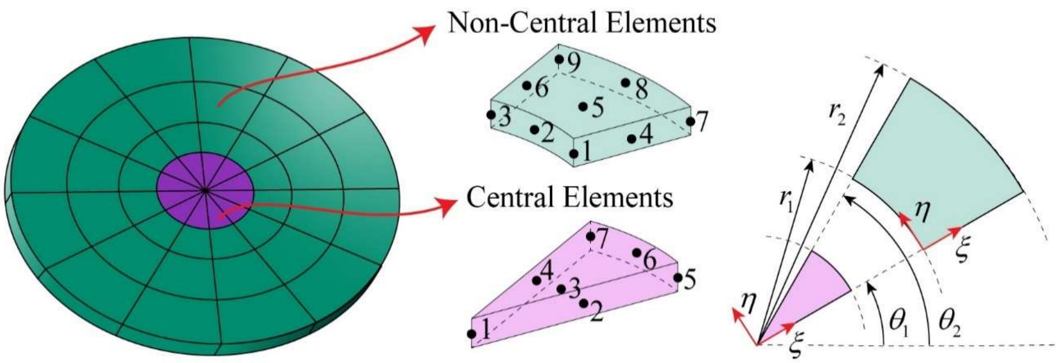

Fig. 2: A schematic of the discretization process for a circular plate with central and non-central elements

Subsequently, the relations will first be presented for the non-central element. The following dimensionless variables are defined for the radial and angular positions:

$$\xi = \frac{r - r_1}{r_2 - r_1}, \quad (0 \le \xi \le 1) \qquad \eta = \frac{\theta - \theta_1}{\theta_2 - \theta_1}, \quad (0 \le \eta \le 1) \tag{17}$$

Each component of the displacement field can be related to the degrees of freedom of the nodes as follows:

$$\Lambda(\xi, \eta) = \sum_{i=1}^{9} N_i(\xi, \eta)\, \Lambda_i \tag{18}$$

where Λ can be any of the displacement field variables $(u_0, v_0, w_0, \psi_r, \psi_\theta)$. Additionally, the Lagrange interpolation functions $N_i(\xi, \eta)$ are calculated as follows:

$$\begin{aligned}
&N_1 = 4\left(\xi - \tfrac{1}{2}\right)(\xi - 1)\left(\eta - \tfrac{1}{2}\right)(\eta - 1) && N_2 = -8\left(\xi - \tfrac{1}{2}\right)(\xi - 1)\eta(\eta - 1) && N_3 = 4\left(\xi - \tfrac{1}{2}\right)(\xi - 1)\eta\left(\eta - \tfrac{1}{2}\right)\\
&N_4 = -8\xi(\xi - 1)\left(\eta - \tfrac{1}{2}\right)(\eta - 1) && N_5 = 16\xi(\xi - 1)\eta(\eta - 1) && N_6 = -8\xi(\xi - 1)\eta\left(\eta - \tfrac{1}{2}\right)\\
&N_7 = 4\xi\left(\xi - \tfrac{1}{2}\right)\left(\eta - \tfrac{1}{2}\right)(\eta - 1) && N_8 = -8\xi\left(\xi - \tfrac{1}{2}\right)\eta(\eta - 1) && N_9 = 4\xi\left(\xi - \tfrac{1}{2}\right)\eta\left(\eta - \tfrac{1}{2}\right)
\end{aligned} \tag{19}$$

The displacement field is interpolated as follows within the element:

$$\begin{aligned}
u_0 &= \lfloor N_u \rfloor \{\Delta_e\}\\
&= [N_1 \;\; 0 \;\; 0 \;\; 0 \;\; 0 \;\; N_2 \;\; 0 \;\; 0 \;\; 0 \;\; 0 \;\; \ldots \;\; N_9 \;\; 0 \;\; 0 \;\; 0 \;\; 0]\{\Delta_e\}\\
v_0 &= \lfloor N_v \rfloor \{\Delta_e\}\\
&= [0 \;\; N_1 \;\; 0 \;\; 0 \;\; 0 \;\; 0 \;\; N_2 \;\; 0 \;\; 0 \;\; 0 \;\; \ldots \;\; 0 \;\; N_9 \;\; 0 \;\; 0 \;\; 0]\{\Delta_e\}\\
w_0 &= \lfloor N_w \rfloor \{\Delta_e\}\\
&= [0 \;\; 0 \;\; N_1 \;\; 0 \;\; 0 \;\; 0 \;\; 0 \;\; N_2 \;\; 0 \;\; 0 \;\; \ldots \;\; 0 \;\; 0 \;\; N_9 \;\; 0 \;\; 0]\{\Delta_e\}\\
\psi_r &= \lfloor N_{\psi_r} \rfloor \{\Delta_e\}\\
&= [0 \;\; 0 \;\; 0 \;\; N_1 \;\; 0 \;\; 0 \;\; 0 \;\; 0 \;\; N_2 \;\; 0 \;\; \ldots \;\; 0 \;\; 0 \;\; 0 \;\; N_9 \;\; 0]\{\Delta_e\}\\
\psi_\theta &= \lfloor N_{\psi_\theta} \rfloor \{\Delta_e\}\\
&= [0 \;\; 0 \;\; 0 \;\; 0 \;\; N_1 \;\; 0 \;\; 0 \;\; 0 \;\; 0 \;\; N_2 \;\; \ldots \;\; 0 \;\; 0 \;\; 0 \;\; 0 \;\; N_9]\{\Delta_e\}
\end{aligned} \tag{20}$$

For the central element, the components of the displacement field can be related to the degrees of freedom of the nodes as follows:

$$\Lambda(\xi,\eta) = \sum_{i=1}^{7} N_i(\xi,\eta)\,\Lambda_i \tag{21}$$

The Lagrange interpolation functions are also calculated as follows:

$$\begin{aligned}
&N_1 = 2\left(\xi-\frac{1}{2}\right)(\xi-1) && N_2 = -8\xi(\xi-1)\left(\eta-\frac{1}{2}\right)(\eta-1) && N_3 = 16\xi(\xi-1)\eta(\eta-1)\\
&N_4 = -8\xi(\xi-1)\eta\left(\eta-\frac{1}{2}\right) && N_5 = 4\xi\left(\xi-\frac{1}{2}\right)\left(\eta-\frac{1}{2}\right)(\eta-1) && N_6 = -8\xi\left(\xi-\frac{1}{2}\right)\eta(\eta-1)\\
&N_7 = 4\xi\left(\xi-\frac{1}{2}\right)\eta\left(\eta-\frac{1}{2}\right)
\end{aligned} \tag{22}$$

The displacement field is also interpolated as follows within the element:

$$\begin{aligned}
u_0 &= [N_u]\{\Delta_e\}\\
&= [N_1\ \ 0\ \ 0\ \ 0\ \ 0\ \ N_2\ \ 0\ \ 0\ \ 0\ \ 0\ \ \ldots\ \ N_7\ \ 0\ \ 0\ \ 0\ \ 0]\{\Delta_e\}\\
v_0 &= [N_v]\{\Delta_e\}\\
&= [0\ \ N_1\ \ 0\ \ 0\ \ 0\ \ 0\ \ N_2\ \ 0\ \ 0\ \ 0\ \ \ldots\ \ 0\ \ N_7\ \ 0\ \ 0\ \ 0]\{\Delta_e\}\\
w_0 &= [N_w]\{\Delta_e\}\\
&= [0\ \ 0\ \ N_1\ \ 0\ \ 0\ \ 0\ \ 0\ \ N_2\ \ 0\ \ 0\ \ \ldots\ \ 0\ \ 0\ \ N_7\ \ 0\ \ 0]\{\Delta_e\}\\
\psi_r &= [N_{\psi_r}]\{\Delta_e\}\\
&= [0\ \ 0\ \ 0\ \ N_1\ \ 0\ \ 0\ \ 0\ \ 0\ \ N_2\ \ 0\ \ \ldots\ \ 0\ \ 0\ \ 0\ \ N_7\ \ 0]\{\Delta_e\}\\
\psi_\theta &= [N_{\psi_\theta}]\{\Delta_e\}\\
&= [0\ \ 0\ \ 0\ \ 0\ \ N_1\ \ 0\ \ 0\ \ 0\ \ 0\ \ N_2\ \ \ldots\ \ 0\ \ 0\ \ 0\ \ 0\ \ N_7]\{\Delta_e\}
\end{aligned} \tag{23}$$

By substituting the displacement field (20) or (23) into Eqs. (5) and (13), it can be written as:

$$T = \frac{1}{2}\{\dot{\Delta}_e\}^T[M_e]\{\dot{\Delta}_e\} \tag{24-a}$$

$$U = \frac{1}{2}\{\Delta_e\}^T[K_e]\{\Delta_e\} \tag{24-b}$$

where $[M_e]$ and $[K_e]$ are the element mass and stiffness matrices, respectively, which are provided in Appendix A. Additionally, $\{\dot{\Delta}_e\}$ is the element velocity vector. It is worth mentioning that the integrals related to the mass and stiffness matrices of the element have been calculated numerically, with the corresponding details provided in Appendix A.

By assembling the mass and stiffness matrices of the different elements and applying the boundary conditions, the governing equations are discretized and written as follows:

$$[M]\{\ddot{\Delta}\} + [K]\{\Delta\} = \{0\} \tag{25}$$

where $[M]$ is the global mass matrix, $[K]$ is the global stiffness matrix, $\{\ddot{\Delta}\}$ is the global acceleration vector, and $\{\Delta\}$ is the global degrees of freedom vector. Assuming the response in the form $\{\Delta\} = \{\Delta_0\}e^{i\omega t}$, where i is the imaginary unit, ω is the frequency of the structural oscillations, and $\{\Delta_0\}$ is the mode shape, and substituting this into Eq. (25) and eliminating the term $e^{i\omega t}$, we will have:

$$([K] - \omega^2[M])\{\Delta_0\} = \{0\} \tag{26}$$

By solving this, the frequencies and mode shapes of the structure can be calculated.

4. Polar Wavelet Transform

In polar coordinates, the signal acquisition is one-dimensional, but due to the circular arrangement of the data acquisition points, the analyzed signal is two-dimensional. Therefore, the polar wavelet transform is a two-dimensional wavelet transform. One of its dimensions is in the direction r, and the other is in the direction θ. Thus, we develop the mathematical relations for these two directions and create a two-dimensional polar wavelet function by the tensor product of them. For the directions r and θ, the wavelet functions $|\psi(r)|$ and $\psi(\theta)$ must have limited energy by nature, because they must perform the convolution operation locally. Mathematically, this property is expressed as follows:

$$\int_{-\infty}^{+\infty} |\psi(r)|\, dr < \infty \qquad \int_{-\infty}^{+\infty} |\psi(\theta)|\, d\theta < \infty \tag{27}$$

Or in other expressions:

$$\|\psi(r)\|^2 < \infty \qquad \|\psi(\theta)\|^2 < \infty \tag{28}$$

$$E_{\psi(r)} = \langle \psi(r), \psi(r) \rangle = \int_{-\infty}^{+\infty} |\psi(r)|^2\, dr < \infty \tag{29}$$

$$E_{\psi(\theta)} = \langle \psi(\theta), \psi(\theta) \rangle = \int_{-\infty}^{+\infty} |\psi(\theta)|^2\, d\theta < \infty \tag{30}$$

The Eqs. (41) and (43) state that $\psi(r)$ and $\psi(\theta)$ are absolutely integrable and square integrable, respectively.

Admissibility condition states that the Fourier transform of a wavelet function cannot contain a zero-frequency component (i.e., $\hat{\psi}(\omega = 0) = 0$):

$$\int_{-\infty}^{+\infty} \frac{|\hat{\psi}(\omega)|^2}{|\omega|}\, d\omega < \infty \tag{31}$$

The wavelets must have zero mean to meet the conditions of admissibility. Mathematically, this property is expressed as follows:

$$\int_{-\infty}^{+\infty} \psi(r)\, dr = 0 \qquad \int_{-\infty}^{+\infty} \psi(\theta)\, d\theta = 0 \tag{32}$$

This condition induces the wavelet function to behave oscillating. In other words, this condition forces the wavelet function to have at least one sign change.

Each wavelet function has its own minimum vanishing moments. If a wavelet function has the vanishing moment(s) n, the following moment equation is valid [4]:

$$M_n = \int_{-\infty}^{+\infty} r^n \psi(r)\, dr = 0\,, n = 0,1, \dots, m \tag{33}$$

$$M_n = \int_{-\infty}^{+\infty} \theta^n \psi(\theta)\, d\theta = 0\,, n = 0, 1, \dots, m \tag{34}$$

The filters used for 2D-DWT must be two-dimensional. These two-dimensional filters are also called kernels or masks. The two-dimensional filters used in 2D-DWT are obtained from the expansion of the one-dimensional scaling function's coefficients and one-dimensional wavelet function's coefficients as follows:

$$\varphi(r,\theta) = \varphi(r)\varphi(\theta) \tag{35}$$

$$\psi^{r}(r,\theta) = \psi(r)\,\varphi(\theta) \tag{36}$$

$$\psi^{\theta}(r,\theta) = \varphi(r)\psi(\theta) \tag{37}$$

$$\psi^{p}(r,\theta) = \psi(r)\;\psi(\theta) \tag{38}$$

5. Optimal Polar Wavelet Selection

A two-dimensional discrete wavelet transform (2D-DWT) is established based on multiresolution analysis for images. In multiresolution analysis for images, we work on two-dimensional signals or images. Thus, singularities or faults in images can have their own directions or forms. As mentioned, the multiresolution analysis for one-dimensional signals follows the following rule:

$$f = A_{\mathrm{J}} + \sum_{m=1}^{J} d_m \tag{39}$$

In multiresolution analysis for a polar function $f(r,\theta)$, we have four subimages: $A_{\mathrm{J}}(r,\theta)$, the approximate sub-image; $d_m^{a}(r,\theta)$, the detail sub-image in the angular direction; d_m^{r}, the detail sub-image in the radial direction; and d_m^{c}, the detail sub-image in the coupled direction. Thus, two-dimensional multiresolution analysis can be expressed as follows:

$$f(r,\theta) = A_{\mathrm{J}}(r,\theta) + \sum_{m=1}^{J} d_m^{a}(r,\theta) + d_m^{r}(r,\theta) + d_m^{c}(r,\theta) \tag{40}$$

Therefore, we can write for the first level of decomposition (Level 1):

$$f(r,\theta) = A_1(r,\theta) + d_1^{a}(r,\theta) + d_1^{r}(r,\theta) + d_1^{c}(r,\theta) \tag{41}$$

As the decomposition level increases, more details of the signal will be available. In addition, the level of approximation of the signal will be higher, which means that the approximation is performed in larger sub-spaces; as a result, the approximation will be less accurate.

Assuming the size of $f(r,\theta)$ is $n \times m$, the following relations are related to the two-dimensional discrete wavelet transform:

$$A^{\phi}{}_{j,n,m}(r,\theta) = \frac{1}{2}\sum_{r=0}^{n-1}\sum_{\theta=0}^{m-1} f(r,\theta)2^{\frac{-j}{2}}\phi\left(2^{-j}r - n, 2^{-j}\theta - m\right) \tag{42}$$

$$D^{r}{}_{j,n,m}(r,\theta) = \frac{1}{2}\sum_{r=0}^{n-1}\sum_{\theta=0}^{m-1} f(r,\theta)2^{\frac{-j}{2}}\psi\left(2^{-j}r - n, 2^{-j}\theta - m\right) \tag{43}$$

$$D^{\theta}{}_{j,n,m}(r,\theta)=\frac{1}{2}\sum_{r=0}^{n-1}\sum_{\theta=0}^{m-1}f(r,\theta)2^{\frac{-j}{2}}\psi(2^{-j}r-n,2^{-j}\theta-m) \tag{44}$$

$$D^{c}{}_{j,n,m}(r,\theta)=\frac{1}{2}\sum_{r=0}^{n-1}\sum_{\theta=\mathbf{0}}^{m-1}f(r,\theta)2^{\frac{-j}{2}}\psi(2^{-j}r-n,2^{-j}\theta-m) \tag{45}$$

Minimum energy ratio for selecting the optimal polar wavelet criterion in three directions r, θ, c and are proposed as follows:

$$(MER^{r})=\frac{\sum_{\boldsymbol{r}}\sum_{\theta}\left|D^{r*}{}_{1,m,n}(r,\theta)\right|^{2}}{\sum_{\boldsymbol{r}}\sum_{\theta}\left|A^{\phi*}{}_{1,m,n}(r,\theta)\right|^{2}} \tag{46}$$

$$(MER^{\theta})=\frac{\sum_{\boldsymbol{r}}\sum_{\theta}\left|D^{\theta*}{}_{1,m,n}(r,\theta)\right|^{2}}{\sum_{\boldsymbol{r}}\sum_{\theta}\left|A^{\phi*}{}_{1,m,n}(r,\theta)\right|^{2}} \tag{47}$$

$$(MER^{c})=\frac{\sum_{\boldsymbol{r}}\sum_{\theta}\left|D^{\theta*}{}_{1,m,n}(r,\theta)\right|^{2}}{\sum_{\boldsymbol{r}}\sum_{\theta}\left|A^{\phi*}{}_{1,m,n}(r,\theta)\right|^{2}} \tag{48}$$

where:

$$A^{\phi*}{}_{1,m,n}(r,\theta)=\frac{1}{2}\sum_{r=0}^{n-1}\sum_{\theta=0}^{m-1}f(r,\theta)2^{\frac{-1}{2}}\phi^{*}(2^{-1}r-n,2^{-1}\theta-m) \tag{49}$$

$$D^{r*}{}_{1,m,n}(r,\theta)=\frac{1}{2}\sum_{r=0}^{n-1}\sum_{\theta=0}^{m-1}f(r,\theta)2^{\frac{-1}{2}}\psi^{r*}(2^{-1}r-n,2^{-1}\theta-m) \tag{50}$$

$$D^{\theta*}{}_{1,m,n}(r,\theta)=\frac{1}{2}\sum_{r=0}^{n-1}\sum_{\theta=0}^{m-1}f(r,\theta)2^{\frac{-1}{2}}\psi^{\theta*}(2^{-1}r-n,2^{-1}\theta-m) \tag{51}$$

$$D^{c*}{}_{1,m,n}(r,\theta)=\frac{1}{2}\sum_{r=0}^{n-1}\sum_{\theta=\mathbf{0}}^{m-1}f(r,\theta)2^{\frac{-1}{2}}\psi^{c*}(2^{-1}r-n,2^{-1}\theta-m) \tag{52}$$

where $\phi^{*}(r,\theta)$ is the optimal polar scaling wavelet function; also, $\psi^{r*}(r,\theta)$, $\psi^{\theta*}(r,\theta)$, and $\psi^{c*}(r,\theta)$ are the radial, angular, and coupled polar wavelet functions optimized in terms of the minimum energy ratio (MER), respectively. Therefore, $\psi^{r*}(r,\theta)$, $\psi^{\theta*}(r,\theta)$, and $\psi^{c*}(r,\theta)$ lead to minimum ER in the produced polar wavelet coefficients. In addition, $A^{\phi*}{}_{1,m,n}(r,\theta)$ is polar approximation signal, $D^{r*}{}_{1,m,n}(r,\theta)$ is radial detail signal, $D^{\theta*}{}_{1,m,n}(r,\theta)$ is angular detail signal, and $D^{c*}{}_{1,m,n}(r,\theta)$ is the coupled signal.

Fig. 3 shows flowchart of extracting the MER index vector from the vibration mode shape using the polar wavelet transform. According to the proposed method, the first mode shape of the laminated composite circular plate is transformed into four signals: approximation signal $\phi_i(r,\theta)$, radial detail signal $\psi_i^{r}(r,\theta)$, angular detail signal $\psi_i^{a}(r,\theta)$, and coupled radial-angular detail signal $\psi_i^{c}(r,\theta)$. Then, to identify the damage, MER index vectors are calculated for different wavelet functions and for each detail signal to determine which detail signal (radial, angular, or coupled radial-angular) has the best ability to identify the damage. Finally, the MER index vector with the lowest value is selected as MER^*_{final}, and its lowest value for a given wavelet function is the criterion for determining the optimal wavelet selection. Fig. 3 illustrates the procedure for extracting the MER index from the damaged mode shapes in the radial, circumferential, and coupled radial–circumferential directions. The optimal MER value obtained from each mode is then assembled into the MER vector $\{MER^*_1 \quad \cdots \quad MER^*_i \quad \cdots \quad MER^*_n\}^T$, where the superscript T denotes the transpose.

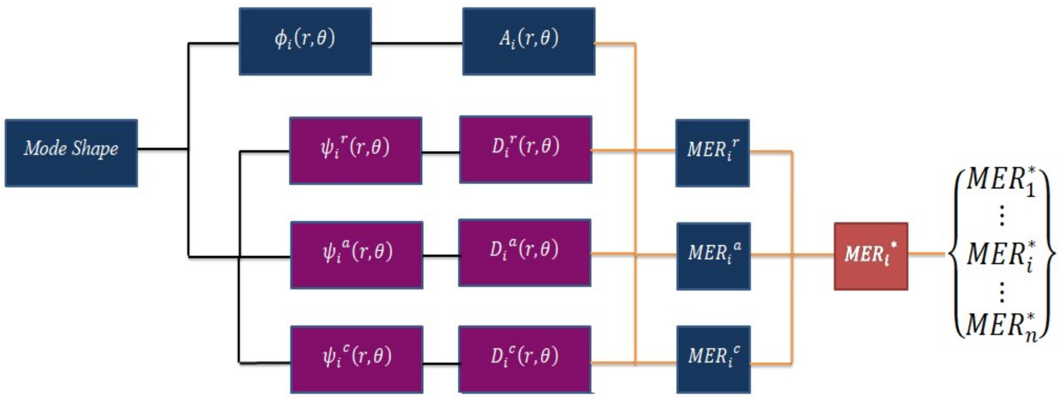

Fig. 3: Flowchart of extracting the MER index vector from the vibration mode shape using the polar wavelet transform

The minimum value of the MER index vector (i.e., MER^*_{final}) is chosen as the criterion for optimal polar wavelet selection:

$$MER^*_{final} = min \begin{Bmatrix} MER^*_1 \\ \vdots \\ MER^*_i \\ \vdots \\ MER^*_n \end{Bmatrix} \tag{53}$$

6. Numerical Analysis

This section addresses numerical analysis in finite element modeling and damage detection. It begins with a convergence study, followed by comparison studies, and then proceeds with numerical damage detection using various damage scenarios based on our proposed methodology. Lastly, experimental damage detection is examined in a glass-epoxy laminated composite disc to validate the method's effectiveness in practical applications.

6.1. Comparative Study

This section presents a convergence study to validate the accuracy of our proposed finite element model. In this section and the following sections, the material properties in the layers are considered as follows, unless explicitly stated otherwise [40,41]:

$$\rho = 1300\frac{kg}{m^3}, \quad E_{22} = 10\,GPa, \quad E_{11} = 20E_{22}, \quad \nu_{12} = 0.25, \\ G_{12} = G_{13} = 0.5E_{22}, \quad G_{23} = 0.2E_{22} \tag{54}$$

The layups [0/90/90/0], $\frac{h}{R} = 0.1$ and clamped boundary conditions have been considered. Table 1 presents the results of the convergence study. The frequencies are dimensionless, expressed as $\bar{\omega} = \frac{\omega R^2}{h}\sqrt{\frac{\rho}{E_{22}}}$. As can be seen, as the number of elements increases, the responses converge. It is worth mentioning that in the subsequent calculations, 15×15 element grid has been used for discretizing the circular plate.

Table 1: Convergence test for the first three dimensionless natural frequencies of the laminated composite circular plate with the layups [0/90/90/0] and the ratio $\frac{h}{R} = 0.1$

Mode No.	5×5	7×7	9×9	11×11	13×13	15×15	17×17
$\bar{\omega}_1$	8.0925	8.0607	8.0448	8.0353	8.0290	8.0281	8.0281
$\bar{\omega}_2$	13.9540	13.8181	13.7479	13.7040	13.6738	13.6721	13.6721
$\bar{\omega}_3$	14.1164	13.9017	13.8019	13.7428	13.7033	13.7011	13.7011

6.2. Comparison Study

In this section, to verify the accuracy of the derived equations and the developed computer programs, the present results are compared with those of others. In Table 2, the results for the isotropic circular plate are compared with the results from references [32] and [33]. For comparison, the frequencies are expressed as $\bar{\bar{\omega}} = \omega R^2\sqrt{\frac{\rho h}{D}}$, where $D = \frac{Eh^3}{12(1-\nu^2)}$.

Table 2: Comparison of the present dimensionless frequencies ($\bar{\bar{\omega}}$) with various references for the isotropic circular plate

Boundary Conditions	$\frac{h}{R}$	Method	Mode No. 1	2	3	4	5
Simply-supported	0.1	Taher et al. [40]	4.8975	13.580	23.722	24.555	28.310
		Hosseini-Hashemi et al. [41]	4.8938	13.5624	-	24.5018	28.240
		Present	4.8973	13.5802	23.5739	24.0795	27.8637
	0.3	Taher et al. [40]	4.6234	7.9234	11.721	16.553	19.452
		Hosseini-Hashemi et al. [41]	4.604	-	11.6264	-	19.2193
		Present	4.6218	-	11.6306	-	19.2260
Clamped	0.1	Taher et al. [40]	9.9908	20.297	32.430	36.743	46.139
		Hosseini-Hashemi et al. [41]	9.9408	20.1765	32.2048	36.4787	45.7730
		Present	9.8727	20.1270	32.1540	36.2580	45.7612
	0.3	Taher et al. [40]	8.4746	15.453	22.766	22.721	25.150
		Hosseini-	8.3553	15.1926	22.2248	-	24.6358

	Hashemi et al. [41]					
	Present	8.2962	15.3745	22.3723	22.3739	24.6856

The frequency results for the laminated composite plate are presented in Tables 3 and 4, and for the clamped boundary condition, they are compared with the results from reference [42]. For the results in Table 3, the following physical properties have been used:

$$\rho = 1600\frac{kg}{m^3},\ E_{22} = 10\,GPa,\quad E_{11} = 20E_{22},\ \ \nu_{12} = 0.25,$$
$$G_{12} = G_{13} = 0.6E_{22},\ \ G_{23} = 0.5E_{22} \tag{55}$$

As can be seen, the results of the present paper align very well with those of others.

Table 3: Comparison of the dimensionless frequencies (ϖ) for laminated composite circular plate with layups [0/90] and $\frac{h}{R} = 0.1$

Mode No.	1	2	3	4	5	6	7	8
Zhang et al. [34]	8.139	12.213	12.213	18.685	18.688	26.812	26.830	28.406
Present	8.138	13.708	14.781	18.874	18.906	27.420	27.424	28.632

Table 4: Comparison of the fundamental frequency (Hz) for laminated composite circular plate with different layups and various $\frac{h}{R}$

$\frac{h}{R}$	Method	[15/15/15/15]	[30/30/30/30]	[45/45/45/45]	[60/60/60/60]
0.005	Zhang et al. [42]	20.382	17.923	15.787	13.606
	Present	21.043	18.210	15.830	13.656
0.01	Zhang et al. [42]	40.708	35.794	31.534	27.182
	Present	41.120	36.031	31.684	27.191
0.02	Zhang et al. [42]	80.987	71.257	62.784	54.129
	Present	81.110	71.362	62.945	54.985
0.03	Zhang et al. [42]	120.42	106.06	93.478	80.613
	Present	120.844	106.356	93.895	80.951

6.3. Numerical Damage Detection

In this section, numerical investigation on the performance of the proposed damage detection method is presented. For this purpose, six different damage scenarios are evaluated according to Table 4.

Fig. 4 shows the damaged first mode shapes corresponding to the six considered damage scenarios. Note that the boundary conditions in all numerical damage scenarios are considered as the clamped boundary condition.

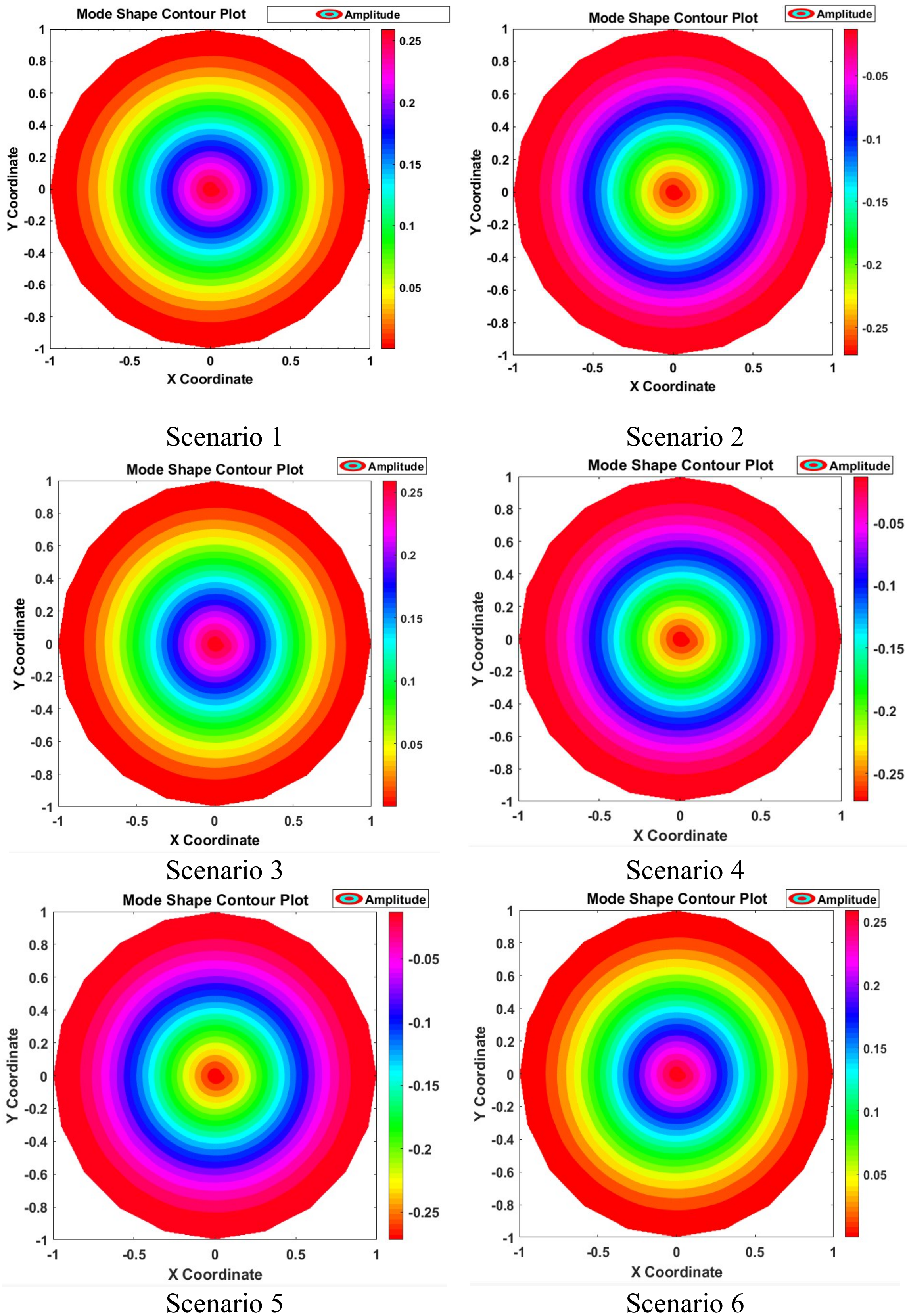

Fig. 4: The damaged first mode shapes corresponding to the six considered damage scenarios

One of the most basic arguments in the literature on damage detection and structural health monitoring is that the presence of damage leads to asymmetry in the geometry of the mode shape. Here again, the absence of perfectly symmetrical contours indicates the presence of damage in the disk. Note that in order to apply damages on the finite element model, before doing assembling operation of the stiffness matrix, a constant called damage index α ($0 < \alpha < 1$) is multiplied by the element's stiffness matrix$[K^e]$ [10]:

$$[Ke]_d = \alpha[Ke] \rightarrow \ D = \frac{[Ke]-[Ke]_d}{[Ke]} \times 100 = \frac{[Ke]-\alpha[Ke]}{[Ke]} \times 100 = (1-\ \alpha)\ \times 100) \qquad (56)$$

where $[K^e]_d$ is the stiffness matrix of a damaged element in the laminated circular plate.

The goal of this section is to discover the wavelet function that minimizes the MER vector when applying a two-dimensional discrete wavelet transform to a signal. Therefore, according to Tables 5 to 7, the minimum energy ratio (MER) index for damage scenarios 1 to 6 using three different families of wavelet functions is calculated.

Table 5 shows the minimum energy ratio (MER) index for damage scenarios 1 and 2 using three different families of wavelet functions. Note that the indexes MER^{α}, MER^{r}, and MER^{c} are the minimum energy ratio (MER) indices obtained from the angular, radial, and coupled detail signals. According to Tables 5 and 7, the best detail signal for searching optimal wavelet function is related to the minimum energy ratio of the coupled detail signal (i.e., MER^{c}).

Table 5. Minimum energy ratio (MER) index for damage scenarios 1 and 2 using three different family of wavelet functions

Scenario 1				**Scenario 2**			
Wavelet	**MER^{α}**	**MER^{r}**	**MER^{c}**	**Wavelet**	**MER^{α}**	**MER^{r}**	**MER^{c}**
Haar	9.37×10^{-6}	0.0028	2.58×10^{-7}	Haar	9.36×10^{-6}	0.0028	2.57×10^{-7}
db2	2.77×10^{-6}	2.35E-04	3.86×10^{-8}	db2	2.74×10^{-6}	2.35×10^{-4}	3.84×10^{-8}
db3	1.05×10^{-6}	3.53×10^{-5}	2.42×10^{-8}	db3	1.03×10^{-6}	3.53×10^{-5}	2.37×10^{-8}
db4	5.68×10^{-7}	4.36×10^{-6}	5.68×10^{-7}	db4	5.92×10^{-7}	4.34×10^{-6}	1.06×10^{-8}
db5	7.77×10^{-7}	8.73×10^{-6}	1.97×10^{-8}	db5	8.03×10^{-7}	8.70×10^{-6}	1.67×10^{-8}
sym2	2.77×10^{-6}	2.35E-04	3.86×10^{-8}	sym2	$2.74\text{E}\times 10^{-6}$	2.35×10^{-4}	3.84×10^{-8}
sym3	1.05×10^{-6}	3.53×10^{-5}	2.42×10^{-8}	sym3	1.03×10^{-6}	1.03×10^{-6}	2.37×10^{-8}
sym4	1.52×10^{-6}	2.03×10^{-5}	8.51×10^{-8}	sym4	1.51×10^{-6}	2.02×10^{-5}	8.30×10^{-8}
sym5	1.59×10^{-6}	1.59×10^{-6}	8.89×10^{-8}	sym5	1.52×10^{-6}	4.72×10^{-5}	8.90×10^{-8}
coif1	4.47×10^{-5}	2.56×10^{-6}	9.36×10^{-8}	coif1	2.66×10^{-6}	4.44×10^{-5}	8.88×10^{-8}
coif2	1.31×10^{-6}	1.60×10^{-5}	6.09×10^{-8}	coif2	1.30×10^{-6}	1.59×10^{-5}	6.08×10^{-8}
coif3	1.12×10^{-6}	1.82×10^{-5}	5.08×10^{-8}	coif3	1.12×10^{-6}	1.81×10^{-5}	5.08×10^{-8}
coif4	1.05×10^{-6}	1.89×10^{-5}	4.63×10^{-8}	coif4	1.05×10^{-6}	1.89×10^{-5}	4.62×10^{-8}
coif5	1.02×10^{-6}	1.93×10^{-5}	4.38×10^{-8}	coif5	1.02×10^{-6}	1.92×10^{-5}	4.37×10^{-8}

Table 6 indicates the minimum energy ratio (MER) index for damage scenarios 3 and 4 using three different family of wavelet functions.

Table 6. Minimum energy ratio (MER) index for damage scenarios 3 and 4 using three different family of wavelet functions

Scenario 3	**Scenario 4**

Wavelet	$\mathbf{MER}^{\alpha}$	$\mathbf{MER}^{r}$	$\mathbf{MER}^{c}$	Wavelet	$\mathbf{MER}^{\alpha}$	$\mathbf{MER}^{r}$	$\mathbf{MER}^{c}$
Haar	9.23×10^{-6}	0.0028	2.55×10^{-7}	Haar	9.44×10^{-6}	0.0028	2.57×10^{-7}
db2	2.70×10^{-6}	2.35×10^{-4}	3.83×10^{-8}	db2	2.74×10^{-6}	2.36×10^{-4}	3.83×10^{-8}
db3	1.00×10^{-6}	3.52×10^{-5}	2.37×10^{-8}	db3	1.03×10^{-6}	3.53×10^{-5}	2.37×10^{-8}
db4	5.38×10^{-7}	$4.32\text{E}\times 10^{-6}$	1.03×10^{-8}	db4	5.57×10^{-7}	4.34×10^{-6}	1.04×10^{-8}
db5	7.42×10^{-7}	8.66×10^{-6}	1.57×10^{-8}	db5	9.03×10^{-7}	8.69×10^{-6}	1.45×10^{-8}
sym2	2.70×10^{-6}	2.35×10^{-4}	3.83×10^{-8}	sym2	$2.74\text{E}\times 10^{-6}$	2.36×10^{-4}	3.83×10^{-8}
sym3	1.00×10^{-6}	3.52×10^{-5}	2.37×10^{-8}	sym3	1.03×10^{-6}	3.53×10^{-5}	2.37×10^{-8}
sym4	1.45×10^{-6}	2.01×10^{-5}	8.13×10^{-8}	sym4	1.48×10^{-6}	2.02×10^{-5}	8.16×10^{-8}
sym5	1.50×10^{-6}	4.70×10^{-5}	8.83×10^{-8}	sym5	1.48×10^{-6}	2.02×10^{-5}	8.16×10^{-8}
coif1	2.53×10^{-6}	4.44×10^{-5}	8.63×10^{-8}	coif1	2.63×10^{-6}	4.44×10^{-5}	8.65×10^{-8}
coif2	1.25×10^{-6}	1.58×10^{-5}	5.64×10^{-8}	coif2	1.28×10^{-6}	1.59×10^{-5}	5.68×10^{-8}
coif3	1.06×10^{-6}	1.80×10^{-5}	4.71×10^{-8}	coif3	1.08×10^{-6}	1.81×10^{-5}	4.74×10^{-8}
coif4	9.96×10^{-7}	1.88×10^{-5}	4.30×10^{-8}	coif4	1.01×10^{-6}	1.88×10^{-5}	4.33×10^{-8}
coif5	9.64×10^{-7}	1.91×10^{-5}	4.08×10^{-8}	coif5	9.75×10^{-7}	1.92×10^{-5}	4.10×10^{-8}

Table 7 denotes the minimum energy ratio (MER) index for damage scenarios 5 and 6 using three different family of wavelet functions.

Table 7. Minimum energy ratio (MER) index for damage scenarios 5 and 6 using three different family of wavelet functions

Scenario 5				Scenario 6			
Wavelet	$\mathbf{MER}^{\alpha}$	$\mathbf{MER}^{r}$	$\mathbf{MER}^{c}$	Wavelet	$\mathbf{MER}^{\alpha}$	$\mathbf{MER}^{r}$	$\mathbf{MER}^{c}$
Haar	9.08×10^{-6}	0.0028	2.79×10^{-7}	Haar	9.76×10^{-6}	0.0028	2.75×10^{-7}
db2	2.71×10^{-6}	2.35×10^{-4}	3.84×10^{-8}	db2	3.12×10^{-6}	2.34×10^{-4}	4.20×10^{-8}
db3	1.07×10^{-6}	3.52×10^{-5}	2.57×10^{-8}	db3	1.27×10^{-6}	3.51×10^{-5}	2.47×10^{-8}
db4	7.46×10^{-7}	4.38×10^{-7}	2.30×10^{-8}	db4	8.64×10^{-7}	4.32×10^{-6}	1.17×10^{-8}
db5	1.01×10^{-6}	8.79×10^{-6}	4.93×10^{-8}	db5	1.09×10^{-6}	8.63×10^{-6}	1.65×10^{-8}
sym2	2.71×10^{-6}	2.35×10^{-4}	3.84×10^{-8}	sym2	3.12×10^{-6}	2.34×10^{-4}	4.20×10^{-8}
sym3	1.07×10^{-6}	3.52×10^{-5}	2.57×10^{-8}	sym3	1.27×10^{-6}	3.51×10^{-5}	2.47×10^{-8}
sym4	1.69×10^{-6}	2.02×10^{-5}	1.30×10^{-7}	sym4	1.87×10^{-6}	2.01×10^{-5}	8.21×10^{-8}
sym5	1.66×10^{-6}	4.70×10^{-5}	1.03×10^{-7}	sym5	1.65×10^{-6}	4.69×10^{-5}	9.06×10^{-8}
coif1	2.73×10^{-6}	4.44×10^{-5}	1.58×10^{-7}	coif1	3.35×10^{-6}	4.43×10^{-5}	8.94×10^{-8}
coif2	1.51×10^{-6}	1.59×10^{-5}	1.07×10^{-7}	coif2	1.67×10^{-6}	1.58×10^{-5}	5.70×10^{-8}
coif3	1.29×10^{-6}	1.80×10^{-5}	8.85×10^{-8}	coif3	1.33×10^{-6}	1.79×10^{-5}	4.77×10^{-8}
coif4	1.20×10^{-6}	1.87×10^{-5}	7.94×10^{-8}	coif4	1.20×10^{-6}	1.87×10^{-5}	4.37×10^{-8}
coif5	1.15×10^{-6}	1.90×10^{-5}	7.40×10^{-8}	coif5	1.14×10^{-6}	1.90×10^{-5}	4.16×10^{-8}

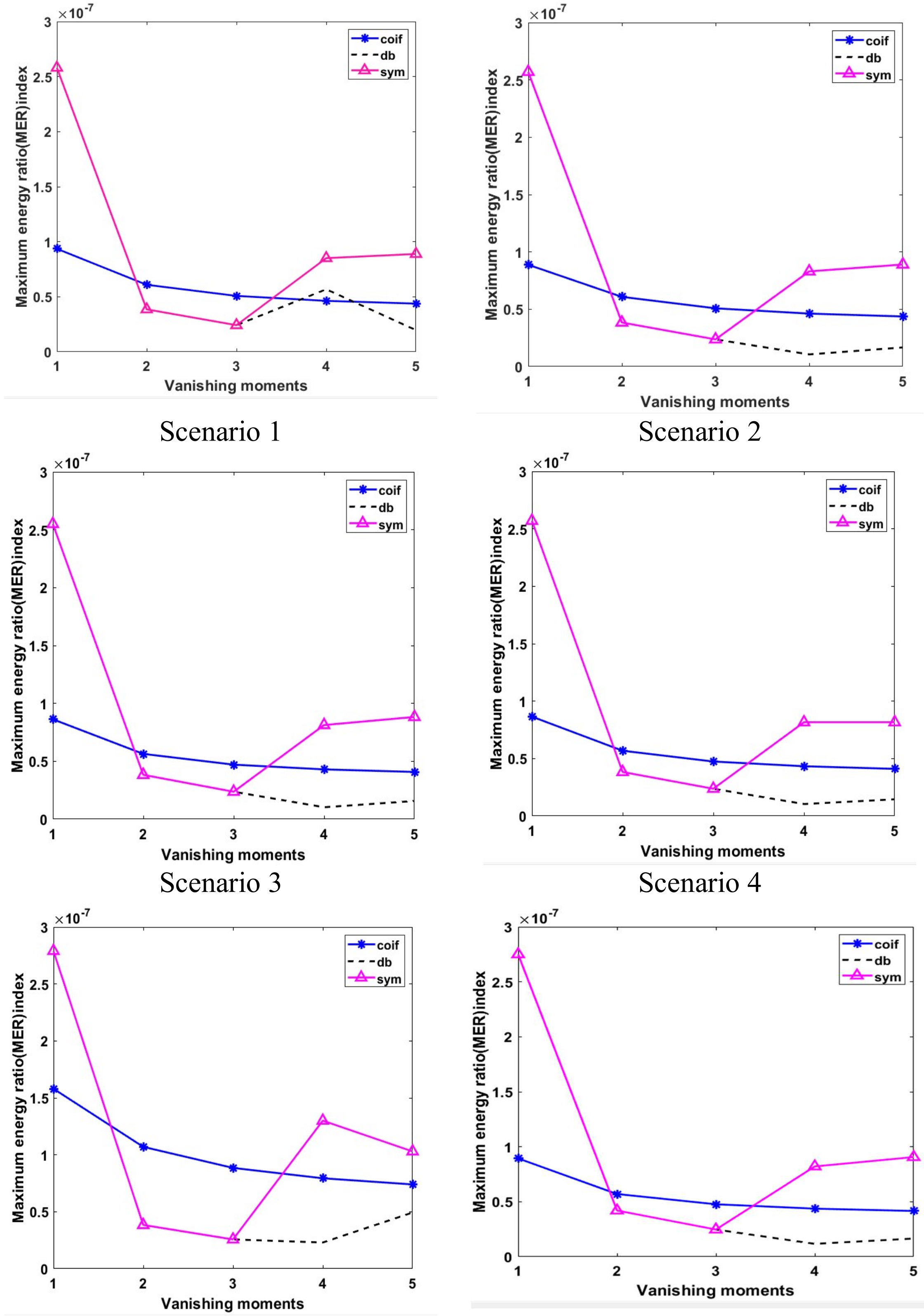

Scenario 1

Scenario 2

Scenario 3

Scenario 4

Scenario 5

Scenario 6

Fig. 5: Results of MER index for coupled details of the six considered damage scenarios

According to Fig. 5 the db wavelet is considered the most optimal wavelet family.

Table 8. Six considered numerical damage scenarios in polar coordinate system

Scenario No.	Damage location		Damage level	Optimal wavelet
	R	θ		
1	8	150°	9%	Db5
2	10	110°	5%	Db4
3	2	0°	10%	Db4
4	3	0°	15%	Db4
5	8	110°	40%	Db4
6	13	335°	70%	Db4

Note that other wavelets from the db family or other families can be found to perform damage detection with high accuracy. However, according to the introduced MER index, the best detail signal for damage detection in the disk under investigation is the coupled detail signal, and the best wavelet family is the db wavelet family. According to Table 8, the optimal wavelet function is db4.

Fig. 6 shows the results of using the conventional wavelet transform to identify the damage of the scenarios presented in Table 8. In Fig. 6, the wavelet functions, as well as one of the three horizontal, vertical, and coupled details are randomly selected to evaluate the performance of the conventional wavelet transform.

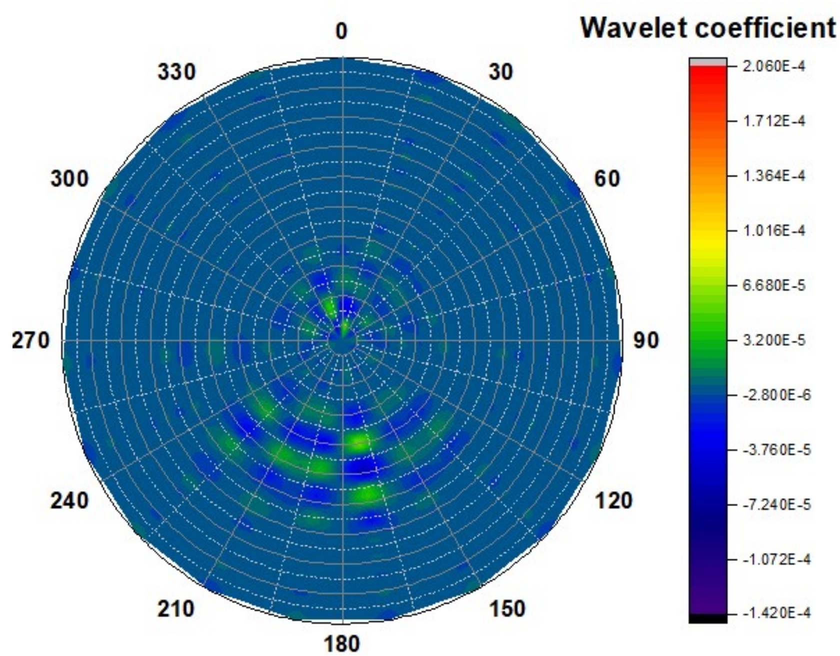

Scenario 1: coupled detail, db2

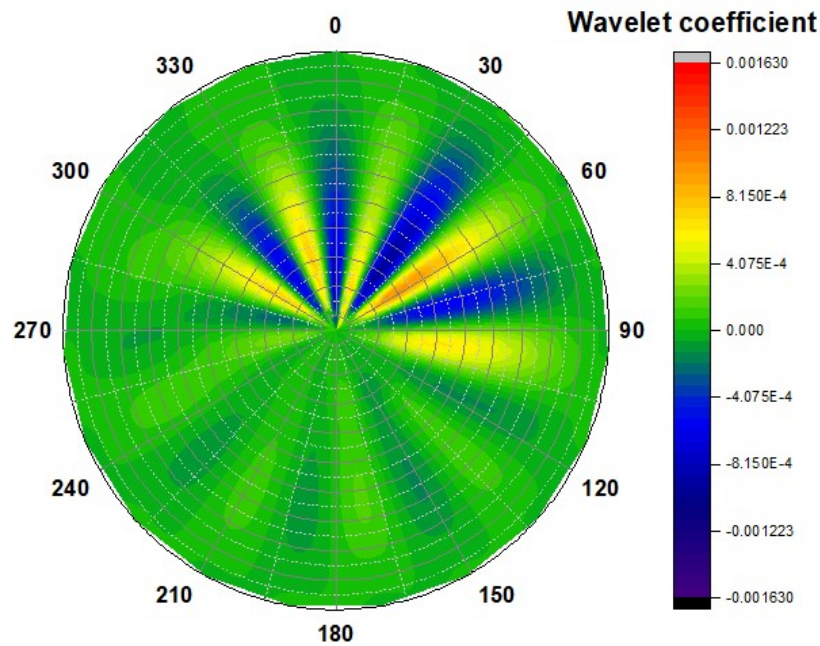

Scenario 2: radial detail, haar

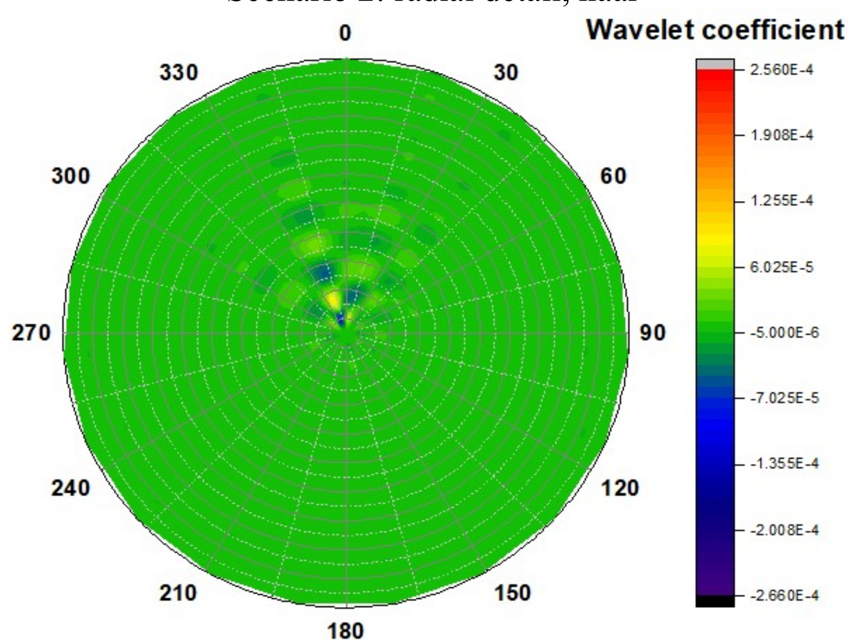

Scenario 3: coupled detail, dmey

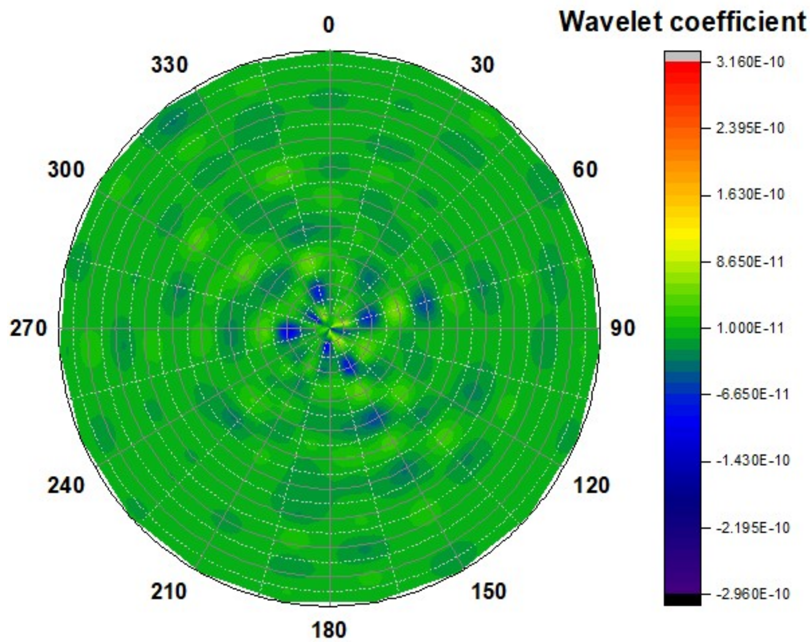

Scenario 4: vertical detail, sym2

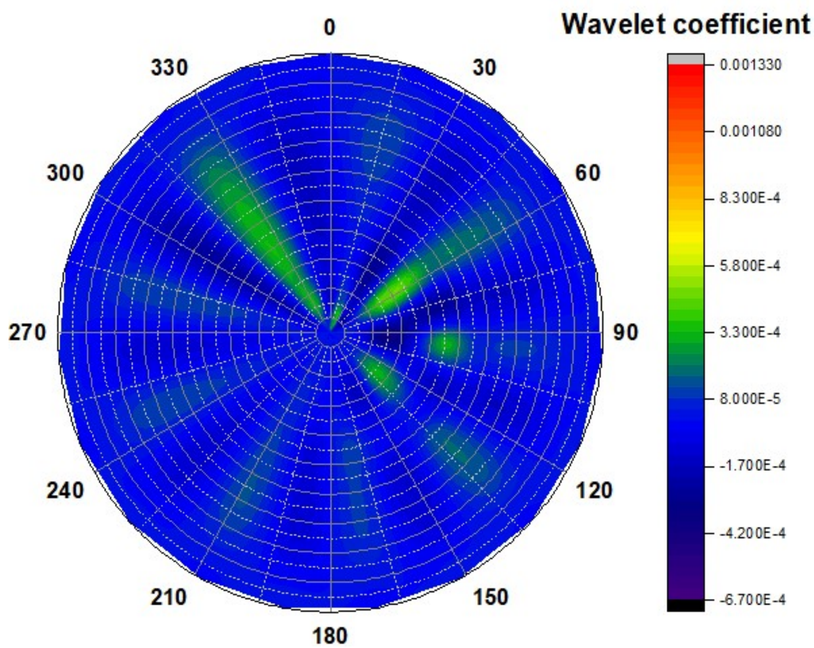

Scenario 5: radial detail, coif2

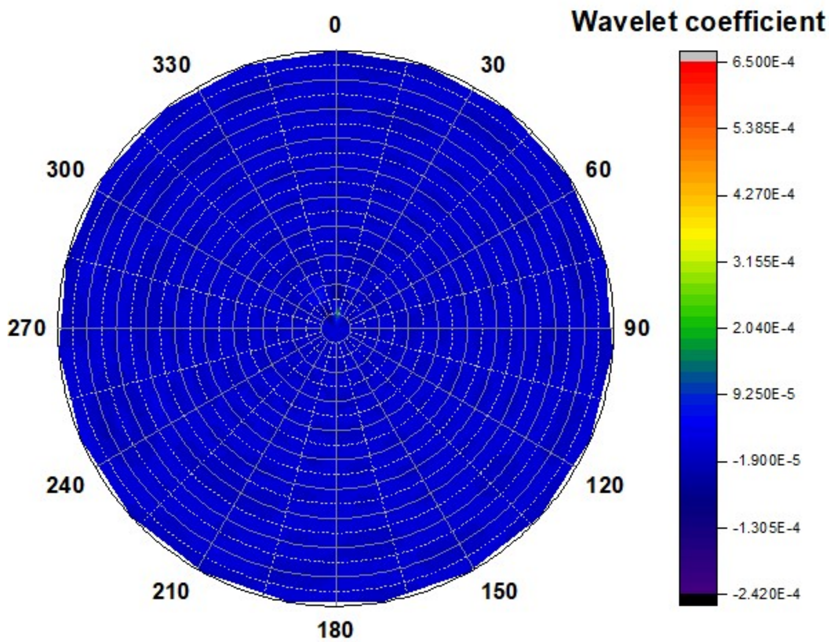

Scenario 6: coupled detail, coif1

Fig. 6. Results of conventional wavelet transform using random wavelet functions and random detail signals

As shown in Fig. 6, damage detection using conventional wavelet transform is performed only using the detail signal. In addition, damage detection using coupled signal is not very high accuracy, because the best wavelet function is not used. Therefore, in order to overcome this weakness, the proposed method is presented. Fig. 7 shows the performance of the proposed methodology in this paper.

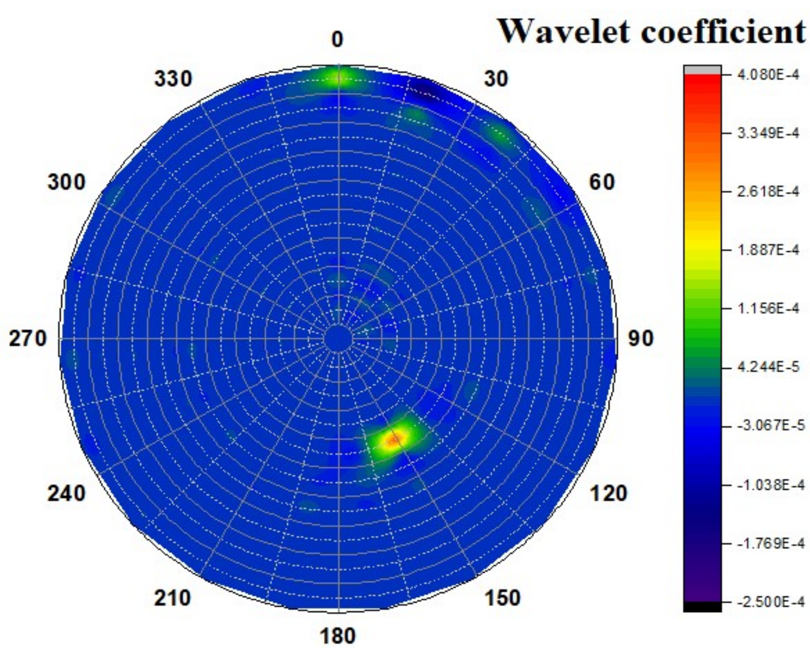

Scenario 1

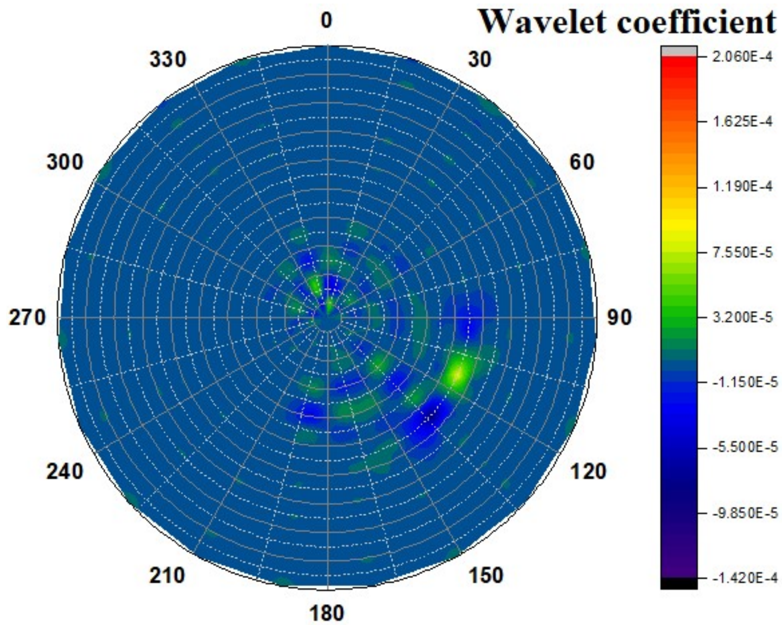

Scenario 2

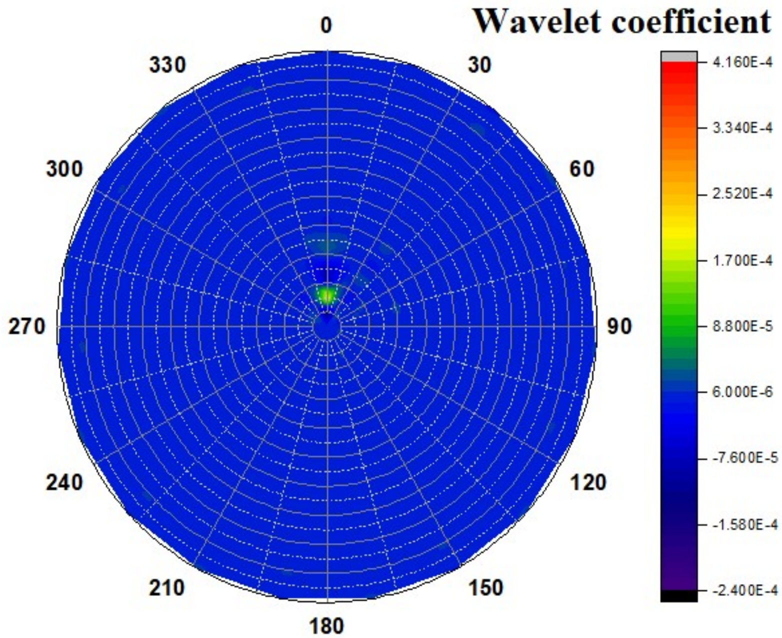

Scenario 3

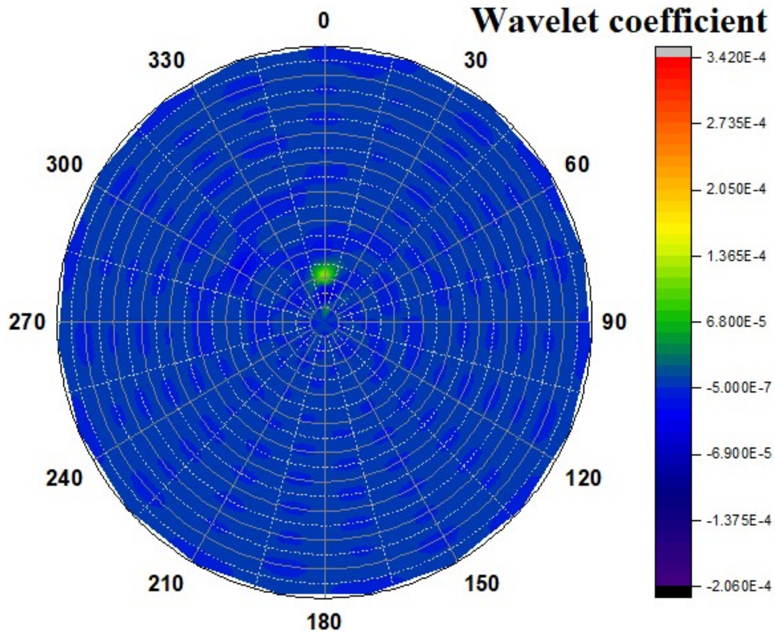

Scenario 4

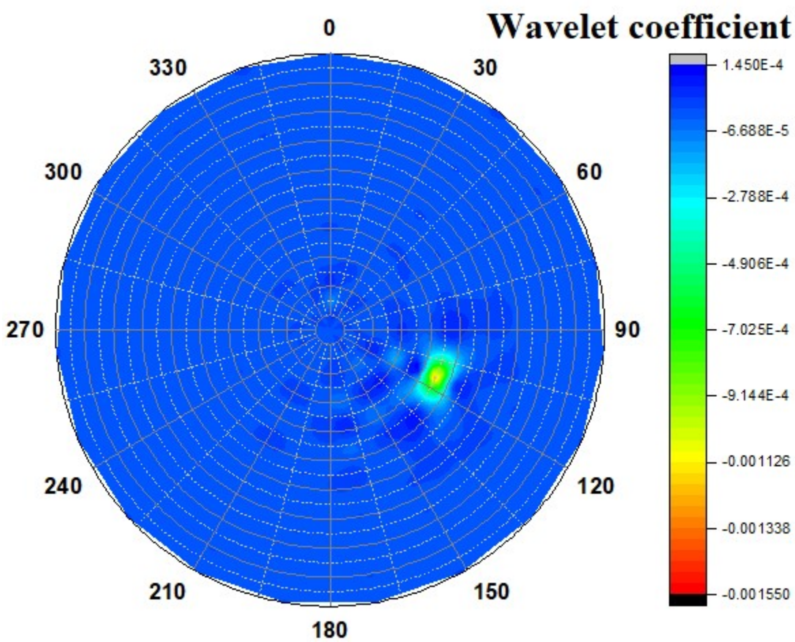

Scenario 5

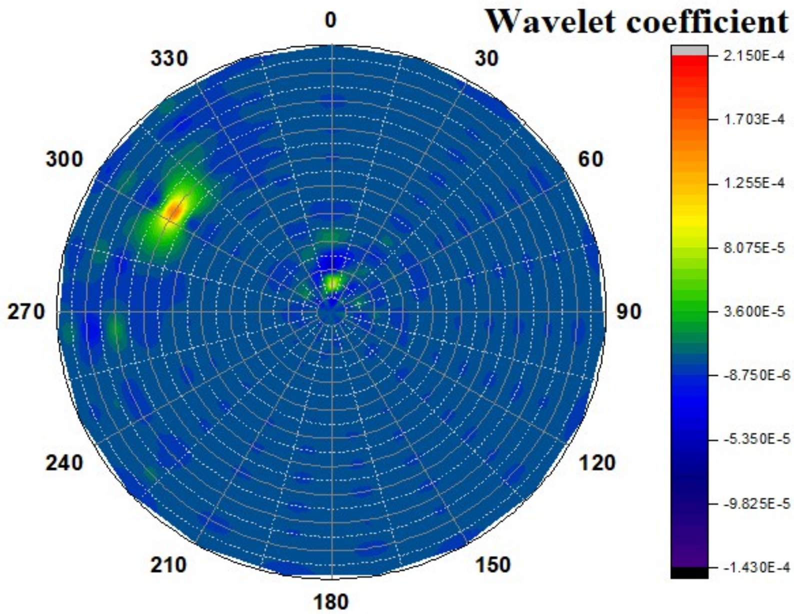

Scenario 6

Fig. 7: Results of damage detection using the proposed methodology

Fig. 7 demonstrates that the proposed methodology accurately identifies damage locations across all scenarios. Note that the coupled detail signal and db5 wavelet function were found to be optimal within this methodology.
Also, to investigate the performance of the proposed methodology under noisy conditions, two noise damage scenarios are examined. For this purpose, scenarios 7 and 8 are considered. In scenario 7, the damage is located at a radius of 8 and an angle of 150 degrees. In scenario 8, the damage is located at a radius of 10 and an angle of 110 degrees. Also, the damage level in the seventh scenario is 9% and in the eighth scenario, it is 5%. Fig. 8 shows the results obtained from damage identification under noisy conditions. The noises obtained from the sum of the mode shape with the Gaussian noise function were obtained with levels of 0.001 and 0.002, respectively, in MATLAB software. Results indicate that the higher the noise level leads to the harder the damage identification, as expected. As the noise level increases, local disturbance caused by damage may be located in the noise neighborhood and lose its singularity in the mode shape signal.

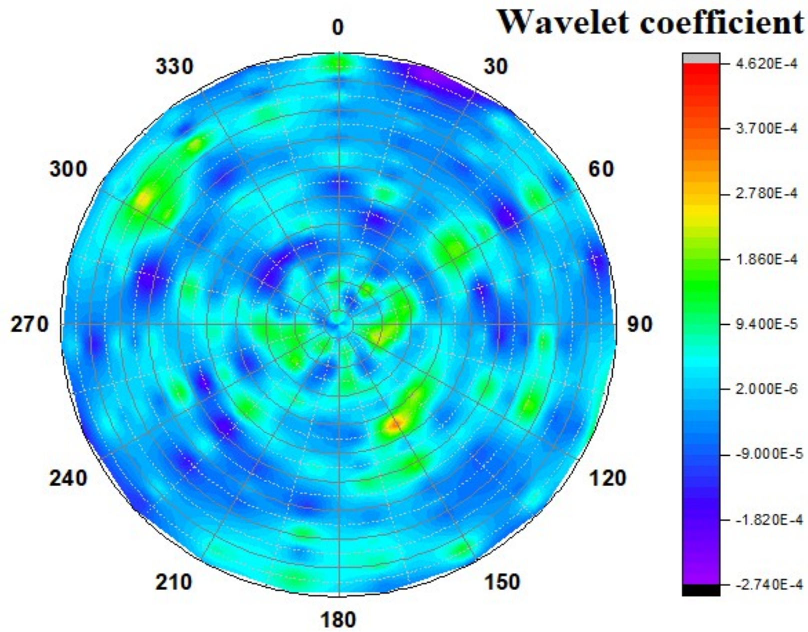

Scenario 7

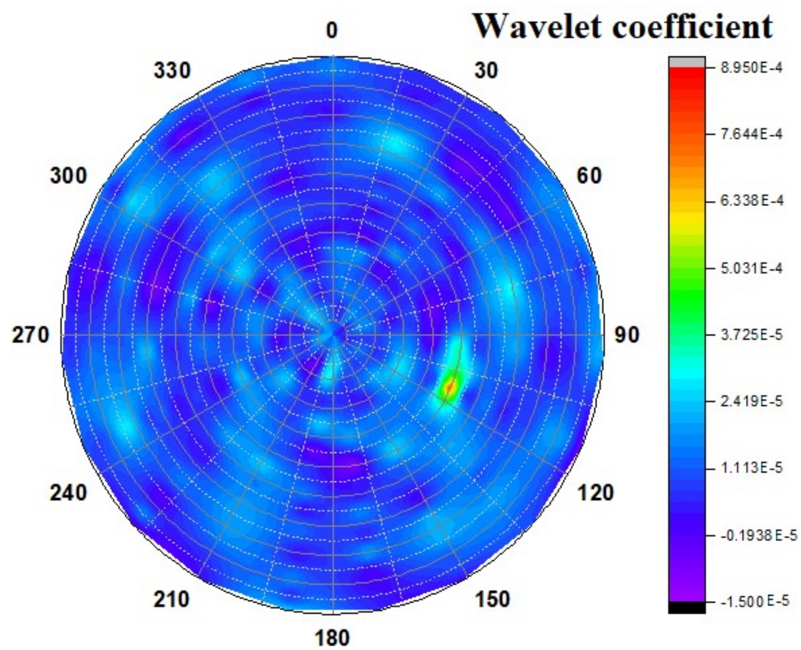

Scenario 8

Fig. 8: The damaged first mode shapes corresponding to the four considered noisy damage scenarios

6.4. Experimental Damage Detection

This section presents experimental results on damage detection to validate the effectiveness of the proposed method for real-world applications. An eight-layer glass-epoxy composite disk is fabricated using the vacuum infusion process (VIP) using Epoxy resin, hardener and glass fabrics, as illustrated in Fig. 9.

Glass fabrics provide cost-effective heat resistance, retaining approximately 50% of their room temperature tensile strength (around 3445 MPa), compressive strength (around 1080 MPa), and elastic modulus (around 73 GPa) [43].

Fig. 9: Fabrication of an eight-layer glass-epoxy laminated composite circular plate using vacuum infusion process (VIP)

Figs. 9a–9i illustrate the fabrication process of an eight-layer glass–epoxy laminated composite circular plate manufactured using the vacuum infusion process. The procedure begins with cutting the glass fiber cloth into circular shapes (Fig. 9a), followed by placing circular Dacron fabric layers on the glass fibers (Fig. 9b). The flat mold bed and its boundary conditions are shown in Fig.

9c. The application of vacuum and the removal of air from the mold chamber are depicted in Fig. 9d. Figs. 9e–9i show the infusion of the epoxy resin–hardener mixture and its permeation through the glass fiber layers under vacuum assistance.

Fig. 10a presents the finite element mesh of the manufactured specimen. The relative positioning of the shaker with respect to the specimen and the applied excitation force are shown in Fig. 10b. Finally, Fig. 10c illustrates the experimental setup used for the modal analysis.

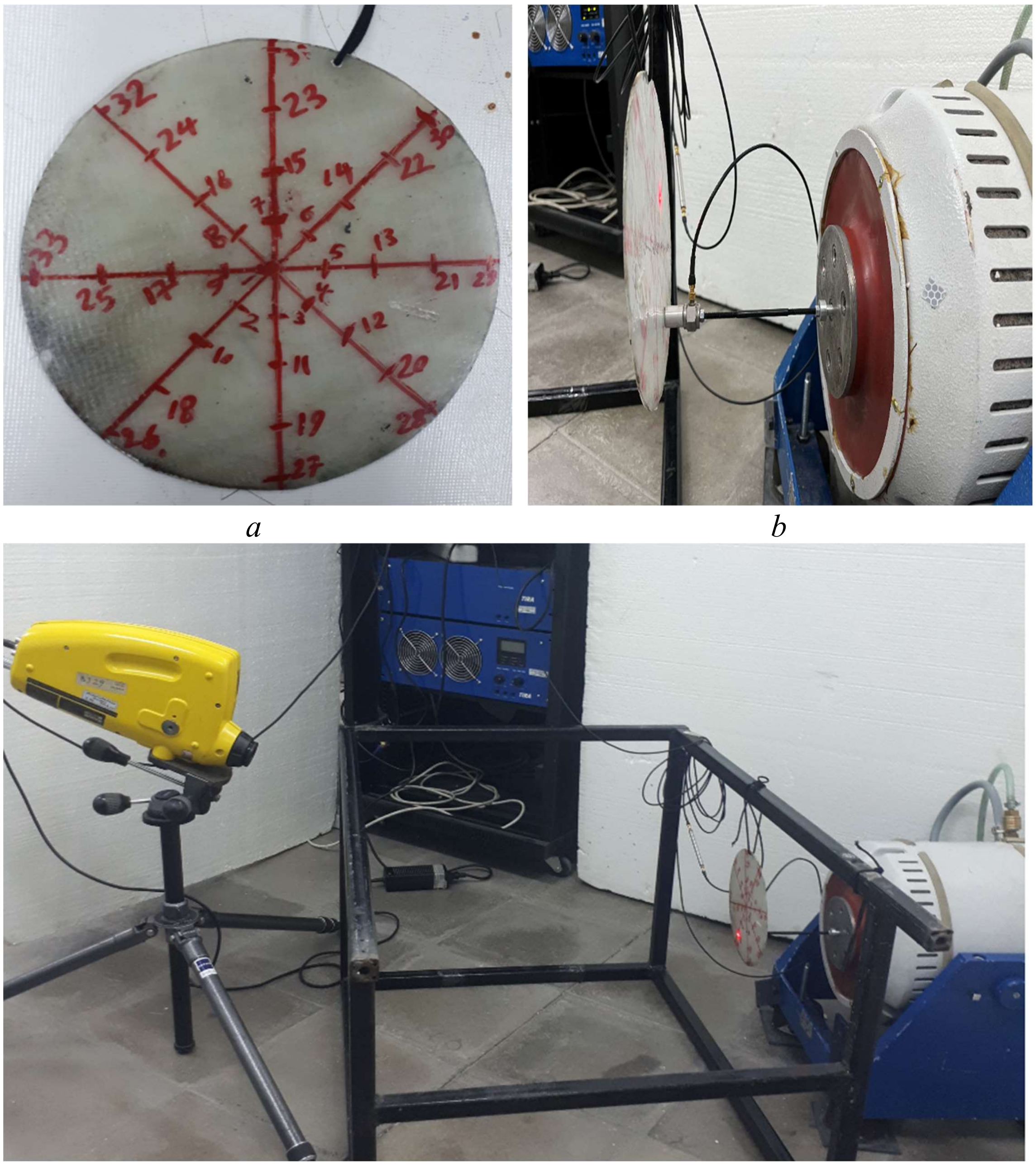

a *b* *c*

Fig. 10: Dividing and modal test of eight-layer glass-epoxy laminated composite

circular plate

Fig. 10 shows dividing and modal test of eight-layer glass-epoxy laminated composite circular plate. The composite circular plate was suspended using a soft elastic to facilitate testing. A laser vibrometer measured velocity by scanning all points on the structure. A vibrating shaker, coupled with an 8200BK force gauge and a 2647A amplifier, applied force. With the composite plate divided into 33 points (Fig. 10a), the shaker was fixed at point 18, and the laser vibrometer measured the response at all points.

A groove measuring 20 mm in length and 3 mm in width was introduced into the laminated composite circular plate at a radial distance of 50 mm from the center and oriented at an angle of 105°, within the sector bounded by points 12, 13, 21, and 20 (Fig. 10a). Modal testing was conducted over the entire plate using a shaker excitation applied at point 18, while the vibration response was measured using a roving laser vibrometer. Frequency response functions (FRFs) were obtained in the frequency range of 0–800 Hz using a BK3560D analyzer in conjunction with PULSE 8 software, based on measured force and acceleration signals. The three FRF curves shown in Fig. 11 correspond to repeated measurements performed under identical test conditions, demonstrating the repeatability and reliability of the experimental data.

In modal analysis, mode shapes are extracted from the measured FRFs through a curve-fitting procedure. Specifically, modal identification software such as ICATS first determines the global modal parameters, including natural frequencies and damping ratios, from the resonant peaks of the FRFs. Subsequently, the relative motion between measurement points is obtained by evaluating the residue (response amplitude) at each location. By assembling these relative amplitudes into a modal vector, the structural deformation pattern corresponding to each mode shape is reconstructed and visualized in animated form.

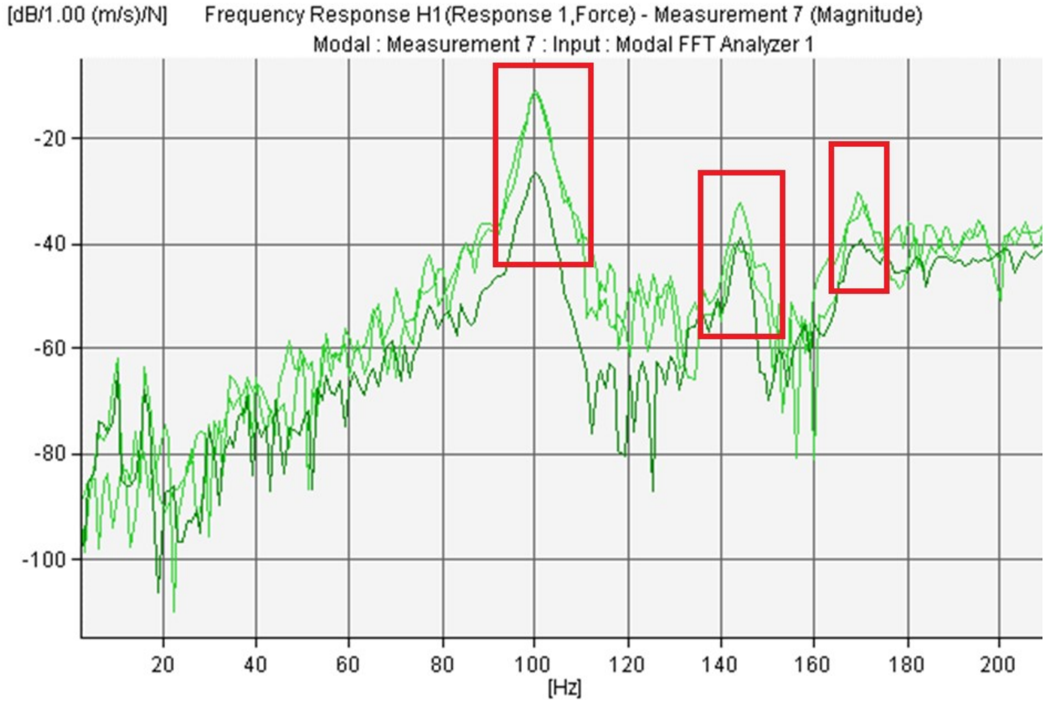

Fig. 11: Frequency response functions obtained from modal testing on damaged laminated composite circular plate in the frequency range of 0 to 200 Hz.

Following the experiment, frequency response functions were analyzed using ICATs software. This analysis yielded the sheet's natural frequencies, damping coefficients, and mode shapes. Table 9 lists the natural frequencies and damping coefficients, while Fig. 12 presents the mode shapes of the damaged laminated composite circular plate.

Table 9. Natural frequencies and damping coefficients of the damaged laminated composite circular plate sheet

Mode No.	1	2	3
Frequency (Hz)	100.43	143.78	172.84

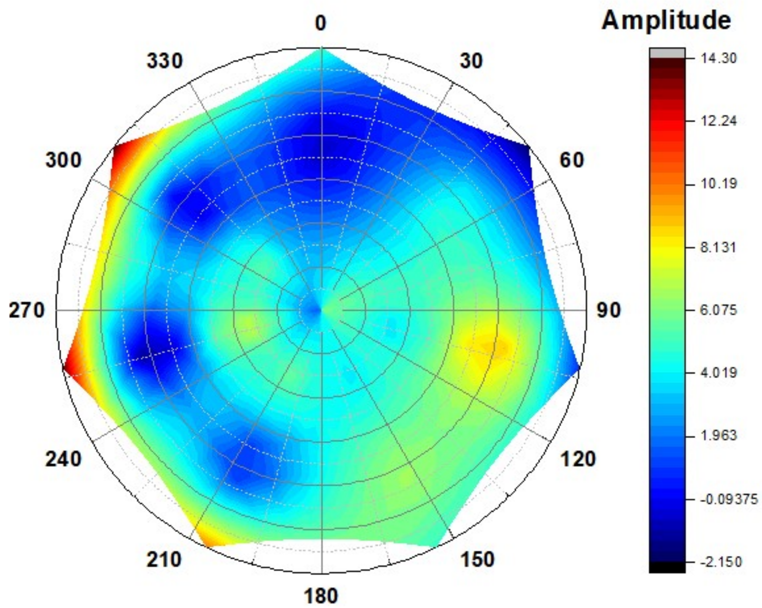

Fig. 12: Experimental mode shape of the constructed eight-layer glass-epoxy laminated composite circular plate

Fig. 13 shows damage detection results on the eight-layer glass-epoxy laminated composite circular plate using a random wavelet function with the coupled detail signal and the coupled detail signal and dmey wavelet (with minimum MER index 0.0160) are used for this experimental scenario.

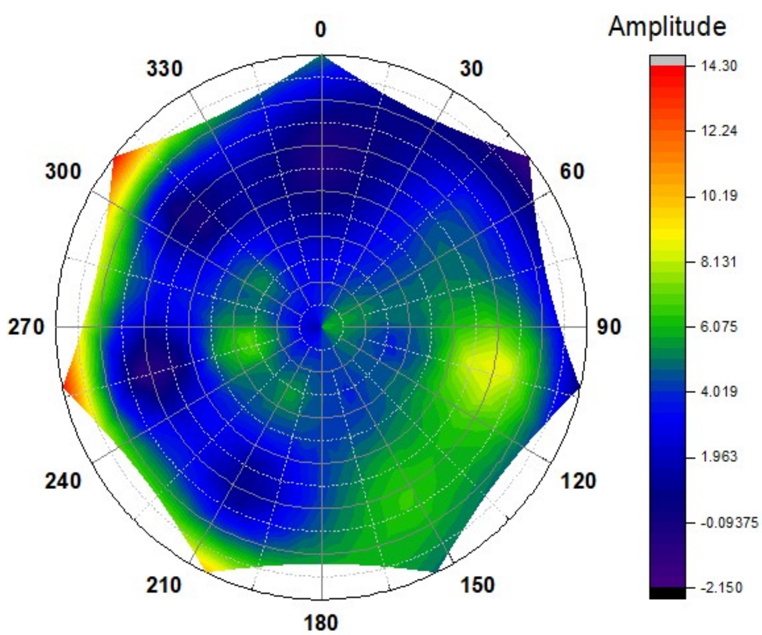

Fig. 13: Results of damage detection on the constructed eight-layer glass-epoxy laminated composite circular plate using a random wavelet function (dmey)

Fig. 14 shows the result of damage detection on the constructed eight-layer glass-epoxy laminated composite circular plate using the proposed method. The coupled detail signal and db4 wavelet (with minimum MER index 4.0410e-04) are used for this experimental scenario.

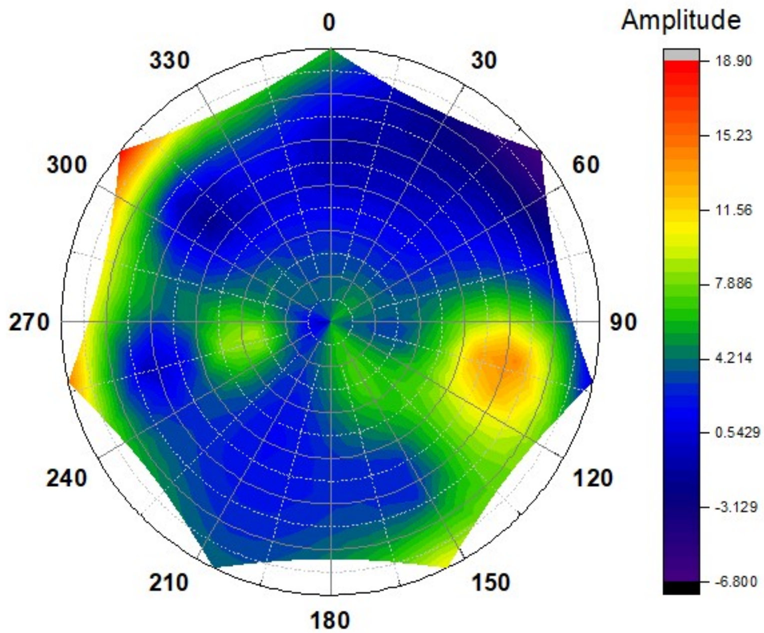

Fig. 14: Result of damage detection on the constructed eight-layer glass-epoxy laminated composite circular plate using the proposed method

7. Conclusions

Circular structures often require sensors arranged circularly for signal processing-based structural health monitoring and damage detection, necessitating signal processing in polar coordinates. This study introduces an optimal polar wavelet transform, based on the discrete two-dimensional wavelet transform, for damage detection in laminated composite circular plates. The transform utilizes wavelet functions in radial, angular, or combined radial-angular directions, optimized using a new minimum Energy Ratio (MER) criterion. The numerical results demonstrated the superior performance of the proposed method (especially for damage below 10%) compared to conventional polar wavelet transforms, as it leverages optimal detail signals and wavelet functions instead of relying on trial-and-error simulations (the optimal detail signal is obtained from the optimal wavelet function and reveals the best information on damage in the structure). Experimental results further validate the effectiveness of the proposed method. According to the findings of this study, the coupled detail signal is the most sensitive polar detail signal to single damage, and as expected, it yields the lowest MER index. Among the optimal wavelet functions that yielded the lowest MER in the coupled detail signal, the

db4 wavelet function was selected. A comparison of the results obtained from the traditional polar wavelet transform (by choosing a random wavelet function) showed that the proposed methodology significantly increases the accuracy of damage detection in polar coordinates. These results were also valid for the experimental findings. Also, according to the findings of this study, the proposed methodology is somewhat robust to environmental noise.
For future work, the present study could be extended to consider damping effects in the numerical model, which may influence the vibration response and the accuracy of damage detection in laminated composite structures. Additionally, the methodology could be adapted to account for delamination as an interlaminar damage mechanism, enabling more comprehensive structural health monitoring of layered composite plates.

Appendix A: Element Mass and Stiffness Matrices
Element Mass Matrix:

$$
\begin{aligned}
[M_e] = \int_0^1 \int_0^1 \Big[& I_1(\lfloor N_u \rfloor^T \lfloor N_u \rfloor + \lfloor N_v \rfloor^T \lfloor N_v \rfloor + \lfloor N_w \rfloor^T \lfloor N_w \rfloor) \\
& + I_2 \left(\lfloor N_u \rfloor^T \left\lfloor N_{\psi_r} \right\rfloor + \left\lfloor N_{\psi_r} \right\rfloor^T \lfloor N_u \rfloor + \lfloor N_v \rfloor^T \left\lfloor N_{\psi_\theta} \right\rfloor + \left\lfloor N_{\psi_\theta} \right\rfloor^T \lfloor N_v \rfloor \right) \\
& + I_3 \left(\left\lfloor N_{\psi_r} \right\rfloor^T \left\lfloor N_{\psi_r} \right\rfloor + \left\lfloor N_{\psi_\theta} \right\rfloor^T \left\lfloor N_{\psi_\theta} \right\rfloor \right) \Big] \theta_{21} d\eta \; (r_1 + r_{21}\xi) d\xi
\end{aligned}
\tag{A.1}
$$

in which $\theta_{21} = \theta_2 - \theta_1$ and $r_{21} = r_2 - r_1$.
Element Stiffness Matrix:

$$
\begin{aligned}
[K] = \int_0^1 \int_0^1 \Big[& \frac{A_{11}}{r_{21}^2} \lfloor N_{u,\xi} \rfloor^T \lfloor N_{u,\xi} \rfloor \\
& + \frac{A_{22}}{(r_1 + r_{21}\xi)^2} \Big(\lfloor N_u \rfloor^T \lfloor N_u \rfloor + \frac{1}{\theta_{21}^2} \lfloor N_{v,\eta} \rfloor^T \lfloor N_{v,\eta} \rfloor + \frac{1}{\theta_{21}} \lfloor N_u \rfloor^T \lfloor N_{v,\eta} \rfloor \\
& + \frac{1}{\theta_{21}} \lfloor N_{v,\eta} \rfloor^T \lfloor N_u \rfloor \Big) \\
+ A_{66} \Big(& \frac{1}{\theta_{21}^2 (r_1 + r_{21}\xi)^2} \lfloor N_{u,\eta} \rfloor^T \lfloor N_{u,\eta} \rfloor + \frac{1}{(r_1 + r_{21}\xi)^2} \lfloor N_v \rfloor^T \lfloor N_v \rfloor \\
& - \frac{1}{\theta_{21}(r_1 + r_{21}\xi)^2} \lfloor N_{u,\eta} \rfloor^T \lfloor N_v \rfloor - \frac{1}{\theta_{21}(r_1 + r_{21}\xi)^2} \lfloor N_v \rfloor^T \lfloor N_{u,\eta} \rfloor \\
& + \frac{1}{r_{21}^2} \lfloor N_{v,\xi} \rfloor^T \lfloor N_{v,\xi} \rfloor \\
& + \frac{1}{(r_1 + r_{21}\xi) r_{21} \theta_{21}} \left(\lfloor N_{u,\eta} \rfloor^T \lfloor N_{v,\xi} \rfloor + \lfloor N_{v,\xi} \rfloor^T \lfloor N_{u,\eta} \rfloor \right) \\
& - \frac{1}{(r_1 + r_{21}\xi) r_{21}} \left(\lfloor N_v \rfloor^T \lfloor N_{v,\xi} \rfloor + \lfloor N_{v,\xi} \rfloor^T \lfloor N_v \rfloor \right) \Big)
\end{aligned}
\tag{A.2}
$$

$$
\begin{aligned}
&+\frac{D_{11}}{r_{21}^2}\lfloor N_{\psi_r,\xi}\rfloor^T\lfloor N_{\psi_r,\xi}\rfloor \\
&\qquad +\frac{D_{22}}{(r_1+r_{21}\xi)^2}\left(\lfloor N_{\psi_r}\rfloor^T\lfloor N_{\psi_r}\rfloor+\frac{1}{\theta_{21}^2}\lfloor N_{\psi_\theta,\eta}\rfloor^T\lfloor N_{\psi_\theta,\eta}\rfloor\right. \\
&\qquad \left.+\frac{1}{\theta_{21}}\lfloor N_{\psi_r}\rfloor^T\lfloor N_{\psi_\theta,\eta}\rfloor+\frac{1}{\theta_{21}}\lfloor N_{\psi_\theta,\eta}\rfloor^T\lfloor N_{\psi_r}\rfloor\right) \\
&+D_{66}\left(\frac{1}{\theta_{21}^2(r_1+r_{21}\xi)^2}\lfloor N_{\psi_r,\eta}\rfloor^T\lfloor N_{\psi_r,\eta}\rfloor+\frac{1}{(r_1+r_{21}\xi)^2}\lfloor N_{\psi_\theta}\rfloor^T\lfloor N_{\psi_\theta}\rfloor\right. \\
&\qquad -\frac{1}{\theta_{21}(r_1+r_{21}\xi)^2}\lfloor N_{\psi_r,\eta}\rfloor^T\lfloor N_{\psi_\theta}\rfloor-\frac{1}{\theta_{21}(r_1+r_{21}\xi)^2}\lfloor N_{\psi_\theta}\rfloor^T\lfloor N_{\psi_r,\eta}\rfloor \\
&\qquad +\frac{1}{r_{21}^2}\lfloor N_{\psi_\theta,\xi}\rfloor^T\lfloor N_{\psi_\theta,\xi}\rfloor \\
&\qquad +\frac{1}{(r_1+r_{21}\xi)r_{21}\theta_{21}}\left(\lfloor N_{\psi_r,\eta}\rfloor^T\lfloor N_{\psi_\theta,\xi}\rfloor+\lfloor N_{\psi_\theta,\xi}\rfloor^T\lfloor N_{\psi_r,\eta}\rfloor\right) \\
&\qquad \left.-\frac{1}{(r_1+r_{21}\xi)r_{21}}\left(\lfloor N_{\psi_\theta}\rfloor^T\lfloor N_{\psi_\theta,\xi}\rfloor+\lfloor N_{\psi_\theta,\xi}\rfloor^T\lfloor N_{\psi_\theta}\rfloor\right)\right) \\
&+\frac{A_{12}}{(r_1+r_{21}\xi)r_{21}}\left(\lfloor N_{u,\xi}\rfloor^T\lfloor N_u\rfloor+\lfloor N_u\rfloor^T\lfloor N_{u,\xi}\rfloor\right) \\
&\qquad +\frac{A_{12}}{(r_1+r_{21}\xi)r_{21}\theta_{21}}\left(\lfloor N_{u,\xi}\rfloor^T\lfloor N_{v,\eta}\rfloor+\lfloor N_{v,\eta}\rfloor^T\lfloor N_{u,\xi}\rfloor\right) \\
&\qquad +\frac{A_{16}}{(r_1+r_{21}\xi)r_{21}\theta_{21}}\left(\lfloor N_{u,\eta}\rfloor^T\lfloor N_{u,\xi}\rfloor+\lfloor N_{u,\xi}\rfloor^T\lfloor N_{u,\eta}\rfloor\right) \\
&\qquad -\frac{A_{16}}{(r_1+r_{21}\xi)r_{21}}\left(\lfloor N_{u,\xi}\rfloor^T\lfloor N_v\rfloor+\lfloor N_v\rfloor^T\lfloor N_{u,\xi}\rfloor\right) \\
&\qquad +\frac{A_{16}}{r_{21}^2}\left(\lfloor N_{u,\xi}\rfloor^T\lfloor N_{v,\eta}\rfloor+\lfloor N_{v,\eta}\rfloor^T\lfloor N_{u,\xi}\rfloor\right) \\
&\quad +\frac{B_{11}}{r_{21}^2}\left(\lfloor N_{u,\xi}\rfloor^T\lfloor N_{\psi_r,\xi}\rfloor+\lfloor N_{\psi_r,\xi}\rfloor^T\lfloor N_{u,\xi}\rfloor\right) \\
&\qquad\quad +\frac{B_{12}}{(r_1+r_{21}\xi)r_{21}}\left(\lfloor N_{u,\xi}\rfloor^T\lfloor N_{\psi_r}\rfloor+\lfloor N_{\psi_r}\rfloor^T\lfloor N_{u,\xi}\rfloor\right) \\
&\qquad\quad +\frac{B_{12}}{(r_1+r_{21}\xi)r_{21}\theta_{21}}\left(\lfloor N_{u,\xi}\rfloor^T\lfloor N_{\psi_\theta,\eta}\rfloor+\lfloor N_{\psi_\theta,\eta}\rfloor^T\lfloor N_{u,\xi}\rfloor\right) \\
&+\frac{B_{16}}{r_{21}}\left(\frac{\lfloor N_{u,\xi}\rfloor^T\lfloor N_{\psi_r,\eta}\rfloor+\lfloor N_{\psi_r,\eta}\rfloor^T\lfloor N_{u,\xi}\rfloor}{(r_1+r_{21}\xi)\,\theta_{21}}-\frac{\lfloor N_{u,\xi}\rfloor^T\lfloor N_{\psi_\theta}\rfloor+\lfloor N_{\psi_\theta}\rfloor^T\lfloor N_{u,\xi}\rfloor}{(r_1+r_{21}\xi)\,r_{21}}\right. \\
&\qquad \left.+\frac{\lfloor N_{u,\xi}\rfloor^T\lfloor N_{\psi_\theta,\eta}\rfloor+\lfloor N_{\psi_\theta,\eta}\rfloor^T\lfloor N_{u,\xi}\rfloor}{r_{21}}\right) \\
&\qquad +\frac{A_{26}}{(r_1+r_{21}\xi)^2}\left(\frac{\lfloor N_u\rfloor^T\lfloor N_{u,\eta}\rfloor+\lfloor N_{u,\eta}\rfloor^T\lfloor N_u\rfloor}{\theta_{21}}-\lfloor N_u\rfloor^T\lfloor N_v\rfloor-\lfloor N_v\rfloor^T\lfloor N_u\rfloor\right. \\
&\qquad \left.+\frac{\lfloor N_{u,\eta}\rfloor^T\lfloor N_{v,\eta}\rfloor+\lfloor N_{v,\eta}\rfloor^T\lfloor N_{u,\eta}\rfloor}{\theta_{21}^2}-\frac{\lfloor N_v\rfloor^T\lfloor N_{v,\eta}\rfloor+\lfloor N_{v,\eta}\rfloor^T\lfloor N_v\rfloor}{\theta_{21}}\right) \\
&\qquad +\frac{A_{26}}{(r_1+r_{21}\xi)}\left(\frac{\lfloor N_u\rfloor^T\lfloor N_{v,\xi}\rfloor+\lfloor N_{v,\xi}\rfloor^T\lfloor N_u\rfloor}{r_{21}}\right. \\
&\qquad \left.+\frac{\lfloor N_{v,\xi}\rfloor^T\lfloor N_{v,\eta}\rfloor+\lfloor N_{v,\eta}\rfloor^T\lfloor N_{v,\xi}\rfloor}{r_{21}\,\theta_{21}}\right)
\end{aligned}
$$

$$
\begin{aligned}
&+\frac{B_{12}}{(r_1+r_{21}\xi)r_{21}}\left(\lfloor N_u\rfloor^T\lfloor N_{\psi_r,\xi}\rfloor+\lfloor N_{\psi_r,\xi}\rfloor^T\lfloor N_u\rfloor+\frac{\lfloor N_{v,\eta}\rfloor^T\lfloor N_{\psi_r,\xi}\rfloor+\lfloor N_{\psi_r,\xi}\rfloor^T\lfloor N_{v,\eta}\rfloor}{\theta_{21}}\right)\\
&\qquad+\frac{B_{22}}{(r_1+r_{21}\xi)^2}\Bigg(\lfloor N_u\rfloor^T\lfloor N_{\psi_r}\rfloor+\lfloor N_{\psi_r}\rfloor^T\lfloor N_u\rfloor\\
&\qquad+\frac{\lfloor N_u\rfloor^T\lfloor N_{\psi_\theta,\eta}\rfloor+\lfloor N_{\psi_\theta,\eta}\rfloor^T\lfloor N_u\rfloor}{\theta_{21}}+\frac{\lfloor N_{v,\eta}\rfloor^T\lfloor N_{\psi_r}\rfloor+\lfloor N_{\psi_r}\rfloor^T\lfloor N_{v,\eta}\rfloor}{\theta_{21}}\\
&\qquad+\frac{\lfloor N_{v,\eta}\rfloor^T\lfloor N_{\psi_\theta,\eta}\rfloor+\lfloor N_{\psi_\theta,\eta}\rfloor^T\lfloor N_{v,\eta}\rfloor}{\theta_{21}^2}\Bigg)\\
&+\frac{B_{26}}{(r_1+r_{21}\xi)^2}\Bigg(\frac{\lfloor N_u\rfloor^T\lfloor N_{\psi_r,\eta}\rfloor+\lfloor N_{\psi_r,\eta}\rfloor^T\lfloor N_u\rfloor}{\theta_{21}}-\lfloor N_u\rfloor^T\lfloor N_{\psi_\theta}\rfloor-\lfloor N_{\psi_\theta}\rfloor^T\lfloor N_u\rfloor\\
&\qquad+\frac{\lfloor N_{v,\eta}\rfloor^T\lfloor N_{\psi_r,\eta}\rfloor+\lfloor N_{\psi_r,\eta}\rfloor^T\lfloor N_{v,\eta}\rfloor}{\theta_{21}^2}-\frac{\lfloor N_{v,\eta}\rfloor^T\lfloor N_{\psi_\theta}\rfloor+\lfloor N_{\psi_\theta}\rfloor^T\lfloor N_{v,\eta}\rfloor}{\theta_{21}}\Bigg)\\
&\qquad+\frac{B_{26}}{(r_1+r_{21}\xi)r_{21}}\Bigg(\frac{\lfloor N_u\rfloor^T\lfloor N_{\psi_\theta,\xi}\rfloor+\lfloor N_{\psi_\theta,\xi}\rfloor^T\lfloor N_u\rfloor}{r_{21}}\\
&\qquad+\frac{\lfloor N_{v,\eta}\rfloor^T\lfloor N_{\psi_\theta,\xi}\rfloor+\lfloor N_{\psi_\theta,\xi}\rfloor^T\lfloor N_{v,\eta}\rfloor}{r_{21}\,\theta_{21}}\Bigg)\\
&\qquad+\frac{B_{16}}{r_{21}}\Bigg(\frac{\lfloor N_{u,\eta}\rfloor^T\lfloor N_{\psi_r,\xi}\rfloor+\lfloor N_{\psi_r,\xi}\rfloor^T\lfloor N_{u,\eta}\rfloor}{(r_1+r_{21}\xi)\,\theta_{21}}-\frac{\lfloor N_v\rfloor^T\lfloor N_{\psi_r,\xi}\rfloor+\lfloor N_{\psi_r,\xi}\rfloor^T\lfloor N_v\rfloor}{(r_1+r_{21}\xi)\,r_{21}}\\
&\qquad+\frac{\lfloor N_{v,\xi}\rfloor^T\lfloor N_{\psi_r,\xi}\rfloor+\lfloor N_{\psi_r,\xi}\rfloor^T\lfloor N_{v,\xi}\rfloor}{r_{21}}\Bigg)
\end{aligned}
$$

$$
\begin{aligned}
&+\frac{B_{26}}{(r_1+r_{21}\xi)^2}\left(\frac{\lfloor N_{u,\eta}\rfloor^T\lfloor N_{\psi_r}\rfloor+\lfloor N_{\psi_r}\rfloor^T\lfloor N_{u,\eta}\rfloor}{\theta_{21}}+\frac{\lfloor N_{u,\eta}\rfloor^T\lfloor N_{\psi_\theta,\eta}\rfloor+\lfloor N_{\psi_\theta,\eta}\rfloor^T\lfloor N_{u,\eta}\rfloor}{\theta_{21}^2}\right.\\
&\qquad\left.-\lfloor N_v\rfloor^T\lfloor N_{\psi_r}\rfloor-\lfloor N_{\psi_r}\rfloor^T\lfloor N_v\rfloor-\frac{\lfloor N_v\rfloor^T\lfloor N_{\psi_\theta,\eta}\rfloor+\lfloor N_{\psi_\theta,\eta}\rfloor^T\lfloor N_v\rfloor}{\theta_{21}}\right)\\
&\qquad+\frac{B_{26}}{(r_1+r_{21}\xi)r_{21}}\left(\lfloor N_{v,\eta}\rfloor^T\lfloor N_{\psi_r}\rfloor+\lfloor N_{\psi_r}\rfloor^T\lfloor N_{v,\eta}\rfloor\right.\\
&\qquad\left.+\frac{\lfloor N_{v,\eta}\rfloor^T\lfloor N_{\psi_\theta,\eta}\rfloor+\lfloor N_{\psi_\theta,\eta}\rfloor^T\lfloor N_{v,\eta}\rfloor}{\theta_{21}}\right)\\
&\qquad+\frac{B_{66}}{(r_1+r_{21}\xi)^2}\left(\frac{\lfloor N_{u,\eta}\rfloor^T\lfloor N_{\psi_r,\eta}\rfloor+\lfloor N_{\psi_r,\eta}\rfloor^T\lfloor N_{u,\eta}\rfloor}{\theta_{21}^2}\right.\\
&\qquad-\frac{\lfloor N_{u,\eta}\rfloor^T\lfloor N_{\psi_\theta}\rfloor+\lfloor N_{\psi_\theta}\rfloor^T\lfloor N_{u,\eta}\rfloor}{\theta_{21}}-\frac{\lfloor N_v\rfloor^T\lfloor N_{\psi_r,\eta}\rfloor+\lfloor N_{\psi_r,\eta}\rfloor^T\lfloor N_v\rfloor}{\theta_{21}}\\
&\qquad\left.+\lfloor N_v\rfloor^T\lfloor N_{\psi_\theta}\rfloor+\lfloor N_{\psi_\theta}\rfloor^T\lfloor N_v\rfloor\right)\\
&\qquad+\frac{B_{66}}{(r_1+r_{21}\xi)r_{21}}\left(\frac{\lfloor N_{v,\xi}\rfloor^T\lfloor N_{\psi_r,\eta}\rfloor+\lfloor N_{\psi_r,\eta}\rfloor^T\lfloor N_{v,\xi}\rfloor}{\theta_{21}}-\lfloor N_{v,\eta}\rfloor^T\lfloor N_{\psi_\theta}\rfloor\right.\\
&\qquad-\lfloor N_{\psi_\theta}\rfloor^T\lfloor N_{v,\eta}\rfloor+\frac{\lfloor N_{u,\eta}\rfloor^T\lfloor N_{\psi_\theta,\xi}\rfloor+\lfloor N_{\psi_\theta,\xi}\rfloor^T\lfloor N_{u,\eta}\rfloor}{\theta_{21}}-\lfloor N_v\rfloor^T\lfloor N_{\psi_\theta,\xi}\rfloor\\
&\qquad\left.-\lfloor N_{\psi_\theta,\xi}\rfloor^T\lfloor N_v\rfloor\right)\\
&+\frac{D_{12}}{(r_1+r_{21}\xi)r_{21}}\left(\lfloor N_{\psi_r,\xi}\rfloor^T\lfloor N_{\psi_r}\rfloor+\lfloor N_{\psi_r}\rfloor^T\lfloor N_{\psi_r,\xi}\rfloor\right.\\
&\qquad\left.+\frac{\lfloor N_{\psi_r,\xi}\rfloor^T\lfloor N_{\psi_\theta,\eta}\rfloor+\lfloor N_{\psi_\theta,\eta}\rfloor^T\lfloor N_{\psi_r,\xi}\rfloor}{\theta_{21}}\right)\\
&\qquad+\frac{D_{16}}{(r_1+r_{21}\xi)r_{21}}\left(\frac{\lfloor N_{\psi_r,\xi}\rfloor^T\lfloor N_{\psi_r,\eta}\rfloor+\lfloor N_{\psi_r,\eta}\rfloor^T\lfloor N_{\psi_r,\xi}\rfloor}{\theta_{21}}-\lfloor N_{\psi_r,\xi}\rfloor^T\lfloor N_{\psi_\theta}\rfloor\right.\\
&\qquad\left.-\lfloor N_{\psi_\theta}\rfloor^T\lfloor N_{\psi_r,\xi}\rfloor+\frac{\lfloor N_{\psi_r,\xi}\rfloor^T\lfloor N_{\psi_\theta,\xi}\rfloor+\lfloor N_{\psi_\theta,\xi}\rfloor^T\lfloor N_{\psi_r,\xi}\rfloor}{r_{21}}\right)
\end{aligned}
$$

$$
\begin{aligned}
&+\frac{D_{26}}{(r_1+r_{21}\xi)^2}\left(\frac{\lfloor N_{\psi_{r,\eta}}\rfloor^T\lfloor N_{\psi_r}\rfloor+\lfloor N_{\psi_r}\rfloor^T\lfloor N_{\psi_{r,\eta}}\rfloor}{\theta_{21}}-\lfloor N_{\psi_r}\rfloor^T\lfloor N_{\psi_\theta}\rfloor-\lfloor N_{\psi_\theta}\rfloor^T\lfloor N_{\psi_r}\rfloor\right.\\
&\qquad+\frac{\lfloor N_{\psi_{r,\eta}}\rfloor^T\lfloor N_{\psi_{\theta,\eta}}\rfloor+\lfloor N_{\psi_{\theta,\eta}}\rfloor^T\lfloor N_{\psi_{r,\eta}}\rfloor}{\theta_{21}^2}\\
&\qquad\left.-\frac{\lfloor N_{\psi_{\theta,\eta}}\rfloor^T\lfloor N_{\psi_\theta}\rfloor+\lfloor N_{\psi_\theta}\rfloor^T\lfloor N_{\psi_{\theta,\eta}}\rfloor}{\theta_{21}}\right)\\
&\qquad+\frac{D_{26}}{(r_1+r_{21}\xi)r_{21}}\left(\lfloor N_{\psi_r}\rfloor^T\lfloor N_{\psi_{\theta,\xi}}\rfloor+\lfloor N_{\psi_{\theta,\xi}}\rfloor^T\lfloor N_{\psi_r}\rfloor\right.\\
&\qquad\left.+\frac{\lfloor N_{\psi_{\theta,\eta}}\rfloor^T\lfloor N_{\psi_{\theta,\xi}}\rfloor+\lfloor N_{\psi_{\theta,\xi}}\rfloor^T\lfloor N_{\psi_{\theta,\eta}}\rfloor}{\theta_{21}}\right)\\
&\qquad+\frac{A_{44}}{(r_1+r_{21}\xi)^2\,\theta_{21}^2}\lfloor N_{w,\eta}\rfloor^T\lfloor N_{w,\eta}\rfloor+A_{44}\lfloor N_{\psi_\theta}\rfloor^T\lfloor N_{\psi_\theta}\rfloor\\
&\qquad+\frac{A_{44}}{(r_1+r_{21}\xi)\,\theta_{21}}\left(\lfloor N_{w,\eta}\rfloor^T\lfloor N_{\psi_\theta}\rfloor+\lfloor N_{\psi_\theta}\rfloor^T\lfloor N_{w,\eta}\rfloor\right)\\
&+A_{55}\left(\frac{\lfloor N_{w,\xi}\rfloor^T\lfloor N_{w,\xi}\rfloor}{r_{21}^2}+\left\lfloor N_{\psi_r}\right\rfloor^T\left\lfloor N_{\psi_r}\right\rfloor+\frac{\lfloor N_{w,\xi}\rfloor^T\left\lfloor N_{\psi_r}\right\rfloor+\left\lfloor N_{\psi_r}\right\rfloor^T\lfloor N_{w,\xi}\rfloor}{r_{21}}\right)\\
&\qquad+\frac{A_{45}}{(r_1+r_{21}\xi)\,\theta_{21}}\left(\frac{\lfloor N_{w,r}\rfloor^T\lfloor N_{w,\theta}\rfloor+\lfloor N_{w,\theta}\rfloor^T\lfloor N_{w,r}\rfloor}{r_{21}}+\lfloor N_{w,\theta}\rfloor^T\left\lfloor N_{\psi_r}\right\rfloor\right.\\
&\qquad\left.+\left\lfloor N_{\psi_r}\right\rfloor^T\lfloor N_{w,\theta}\rfloor\right)\\
&\qquad+A_{45}\left(\frac{\lfloor N_{w,r}\rfloor^T\left\lfloor N_{\psi_\theta}\right\rfloor+\left\lfloor N_{\psi_\theta}\right\rfloor^T\lfloor N_{w,r}\rfloor}{r_{21}}+\left\lfloor N_{\psi_\theta}\right\rfloor^T\left\lfloor N_{\psi_r}\right\rfloor\right.\\
&\qquad\left.\left.+\left\lfloor N_{\psi_r}\right\rfloor^T\left\lfloor N_{\psi_\theta}\right\rfloor\right)\right]\theta_{21}d\eta\ \ (r_1+r_{21}\xi)d\xi
\end{aligned}
$$

As previously mentioned, due to the complexities involved in calculating the analytical response of the integrals related to the element's mass and stiffness matrices, a numerical method has been used for their computation. To this end, the radial and angular intervals of the element are divided into N_ξ and N_η segments, respectively. Therefore, in Eqs. A.1 and A.2, $d\xi \approx \Delta\xi = \frac{1}{N_\xi}$ and $d\eta \approx \Delta\eta = \frac{1}{N_\eta}$ can be written. For calculating the above integrals, $\xi_i = i\,\Delta\xi$ $(i = 1,2,..,N_\xi)$ and $\eta_j = j\,\Delta\eta$ $(j = 1,2,..,N_\eta)$ are substituted, and the computed values at these points can be summed together.

References

[1] Azimi, M., Eslamlou, A. D., & Pekcan, G. (2020). Data-driven structural health monitoring and damage detection through deep learning: State-of-the-art review. Sensors, 20(10), 2778.

[2] Mahdian Parrany, A. (2019). Damage detection in circular cylindrical shells using active thermography and 2-D discrete wavelet analysis. Thin-Walled Structures, 136, 34-49.
[3] Zhang, S., He, Y., Gu, Y., He, Y., Wang, H., Wang, H., Yang, R., Chady, T., & Zhou, B. (2025). UAV based defect detection and fault diagnosis for static and rotating wind turbine blade: a review. Nondestructive Testing and Evaluation, 40(4), 1691-1729.
[4] Giurgiutiu, V., & Soutis, C. (2012). Enhanced composites integrity through structural health monitoring. Applied Composite Materials, 19, 813-829.
[5] Pallarés, F. J., Betti, M., Bartoli, G., & Pallarés, L. (2021). Structural health monitoring (SHM) and Nondestructive testing (NDT) of slender masonry structures: A practical review. Construction and Building Materials, 297, 123768.
[6] Huang, Y., Hu, X., Chen, F., Cao, J., He, Y., Ming, Q., Wang, H., Wang, J., & Tang, T. (2026). Dynamic graph meta-learning with multi-sensor spatial dependencies for cross-category small-sample fault diagnosis in ZDJ9-RTAs. Advanced Engineering Informatics, 70, 104132.
[7] Giordano, P. F., Quqa, S., & Limongelli, M. P. (2023). The value of monitoring a structural health monitoring system. Structural safety, 100, 102280.
[8] Vila, J.L.C.R., Carneiro, S. H.S., Goulart, J.N.V., Anflor, C. T.M., & Jorge, A. B. (2024). Wavelet-based numerical investigation on damage localisation and quantification in beams using static deflections and mode shapes, European Journal of Mechanics - A/Solids, 107, 105351.
[9] Xu, L., Wang, X., Wang, Z., & Cao, G. (2025). Hybrid quantum genetic algorithm for structural damage identification. Computer Methods in Applied Mechanics and Engineering, 438, 117866.
[10] Saadatmorad, M., Siavashi, M., Jafari-Talookolaei, R. A., Pashaei, M. H., Khatir, S., & Thanh, C. L. (2021). Multilayer perceptron neural network for damage identification based on dynamic analysis. In Structural Health Monitoring and Engineering Structures: Select Proceedings of SHM&ES 2020 (pp. 29-48). Singapore: Springer Singapore.
[11] Khanahmadi M. (2025). A cutting-edge framework for damage-sensitive feature extraction leveraging modal dynamic flexibility in signal processing-driven structural health monitoring. Thin-Walled Structures, 216, Part A, 113617.
[12] Niu, Y., Wang, W., Su, Y., Jia, F., & Long, X. (2024). Plastic damage prediction of concrete under compression based on deep learning. Acta Mechanica, 235(1), 255-266.
[13] Wang, H., Li, Y., Men, T., & Li, L. (2024). Physically Interpretable Wavelet-Guided Networks with Dynamic Frequency Decomposition for Machine Intelligence Fault Prediction. IEEE Transactions on Systems, Man, and Cybernetics: Systems, 54(8), 4863-4875.

[14] Abbas, M., & Shafiee, M. (2018). Structural health monitoring (SHM) and determination of surface defects in large metallic structures using ultrasonic guided waves. Sensors, 18(11), 3958.
[15] Liu, Y., Su, J., Wang, Z., He, D., Wang, T., & Huang, Q. (2025). Analytical model of flat rolling force for corrugated composite sheet. International Journal of Mechanical Sciences, 297-298, 110327.
[16] Belardi V.G., Fanelli P., & Vivio F. (2021). On the radial bending of shear-deformable composite circular plates with rectilinear orthotropy, European Journal of Mechanics - A/Solids, 86, 104157.
[17] Nikbakt, S. K. M. S. S., Kamarian, S., & Shakeri, M. (2018). A review on optimization of composite structures Part I: Laminated composites. Composite Structures, 195, 158-185.
[18] Prabhakar, M. M., Rajini, N., Ayrilmis, N., Mayandi, K., Siengchin, S., Senthilkumar, K., ... & Ismail, S. O. (2019). An overview of burst, buckling, durability and corrosion analysis of lightweight FRP composite pipes and their applicability. Composite Structures, 230, 111419.
[19] Uwayed, A. N., Brethee, K. F., Muhammad S. O. (2023). Improved vibration based damage detection in laminated composite plate structures under free and forced modal analysis. European Journal of Mechanics - A/Solids, 100, 105031
[20] Saadatmorad, M., Shahavi, M. H., & Gholipour, A. (2024). Damage detection in laminated composite beams reinforced with Nano-particles using covariance of vibration mode shape and wavelet transform. Journal of Vibration Engineering & Technologies, 12(3), 2865-2875.
[21] Liu, D., Tang, Y., & Cong, W. L. (2012). A review of mechanical drilling for composite laminates. Composite structures, 94(4), 1265-1279.
[22] Diamanti, K., & Soutis, C. (2010). Structural health monitoring techniques for aircraft composite structures. Progress in Aerospace Sciences, 46(8), 342-352.
[23] Heshmati, A., Jafari-Talookolaei, R.-A., Valvo, P. S., & Saadatmorad, M. (2023). A novel damage detection technique for laminated composite beams under the action of a moving load. Mechanical Systems and Signal Processing, 202, 110692.
[24] Sohn, H., Park, G., Wait, J. R., Limback, N. P., & Farrar, C. R. (2003). Wavelet-based active sensing for delamination detection in composite structures. Smart Materials and structures, 13(1), 153.
[25] Grabowska, J., Palacz, M., Krawczuk, M., Ostachowicz, W. M., Trendafilova, I., Manoach, E., & Cartmell, M. P. (2007). Wavelet analysis for damage identification in composite structures. Key Engineering Materials, 347, 253-258.
[26] Wang, Q., & Wu, N. (2010). Detecting the delamination location of a beam with a wavelet transform: an experimental study. Smart Materials and Structures, 20(1), 012002.

[27] Yang, Z. B., Radzienski, M., Kudela, P., & Ostachowicz, W. (2016). Scale-wavenumber domain filtering method for curvature modal damage detection. Composite Structures, 154, 396-409.
[28] Sung, D. U., Kim, C. G., & Hong, C. S. (2002). Monitoring of impact damages in composite laminates using wavelet transform. Composites Part B: Engineering, 33(1), 35-43.
[29] Katunin, A., & Holewik, F. (2013). Crack identification in composite elements with non-linear geometry using spatial wavelet transform. Archives of civil and mechanical engineering, 13, 287-296.
[30] Katunin, A., & Przystałka, P. (2014). Damage assessment in composite plates using fractional wavelet transform of modal shapes with optimized selection of spatial wavelets. Engineering Applications of Artificial Intelligence, 30, 73-85.
[31] Knitter-Piątkowska, A., & Guminiak, M. J. (2020). Application of 1-d and 2-d discrete wavelet transform to crack identification in statically and dynamically loaded plates. Engineering Transactions, 68(2), 137-157.
[32] Fan, W., & Qiao, P. (2009). A 2-D continuous wavelet transform of mode shape data for damage detection of plate structures. International journal of solids and structures, 46(25-26), 4379-4395.
[33] Trendafoilova, I., Gorman, D. G., & Manoach, E. (2009). An investigation on vibration-based damage detection in circular plates. Structural Health Monitoring, 8(4), 291-302.
[34] Tufoi, M., Gillich, G. R., Praisach, Z. I., Ntakpe, J. L., & Hatiegan, C. (2014). An analysis of the dynamic behavior of circular plates from a damage detection perspective. Romanian Journal of Acoustics and Vibration, 11(1), 41-46.
[35] Pai, P. F., Oh, Y., & Lee, S. Y. (2002). Detection of defects in circular plates using a scanning laser vibrometer. Structural Health Monitoring, 1(1), 63-88.
[36] Rathod, V. T., & Mahapatra, D. R. (2011). Ultrasonic Lamb wave based monitoring of corrosion type of damage in plate using a circular array of piezoelectric transducers. Ndt & E International, 44(7), 628-636.
[37] Wang, Z., Yan, Y., Gao, Z., & Shi, B. (2024). Inclined crack quantification of plate-like structures based on circular sensor array and lamb waves. Acoustical Physics, 70(3), 560-569.
[38] Giridhara, G., Rathod, V. T., Naik, S., Mahapatra, D. R., & Gopalakrishnan, S. (2010). Rapid localization of damage using a circular sensor array and Lamb wave based triangulation. Mechanical Systems and Signal Processing, 24(8), 2929-2946.
[39] Katunin, A. (2013). Vibration-based damage identification in composite circular plates using polar discrete wavelet transform. Journal of Vibroengineering, 15(1), 355-363.

[40] Taher, H.R.D., Omidi, M., Zadpoor, A.A., & Nikooyan, A.A. (2006). Free vibration of circular and annular plates with variable thickness and different combinations of boundary conditions, Journal of Sound and Vibration, 296, 1084–1092.
[41] Hosseini-Hashemi, Sh., Rezaee, V., Atashipour, S.R., & Girhammar, U.A. (2012). Accurate free vibration analysis of thick laminated circular plates with attached rigid core. Journal of Sound and Vibration, 331, 5581–5596.
[42] Zhang, H., Zhu, R., Shi, D., & Wang, Q. (2019). A simplified plate theory for vibration analysis of composite laminated sector, annular and circular plate. Thin-Walled Structures, 143, 106252.
[43] El-Wazery, M. S., El-Elamy, M. I., & Zoalfakar, S. H. (2017). Mechanical properties of glass fiber reinforced polyester composites. International Journal of Applied Science and Engineering, 14(3), 121-131.